

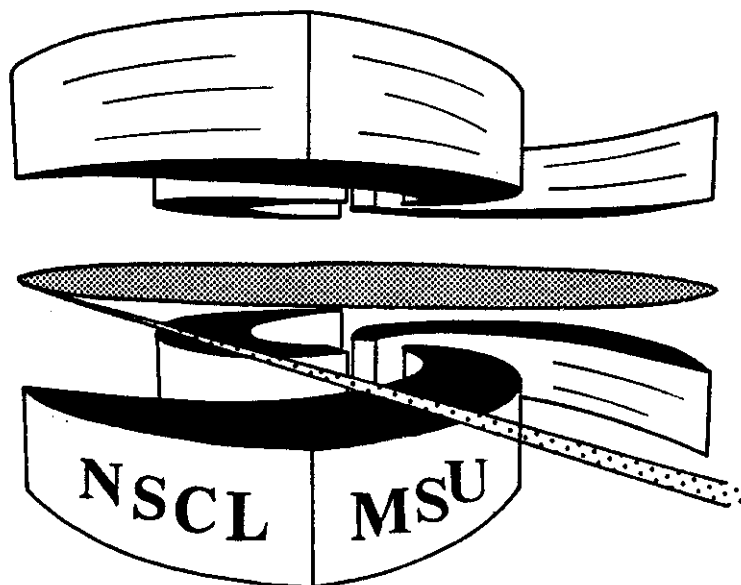


Michigan State University

National Superconducting Cyclotron Laboratory

REACTION PLANE DETERMINATION FOR  
 $^{36}\text{Ar} + ^{197}\text{Au}$  COLLISIONS AT  $E/A = 35$  MeV

M.B. TSANG, R.T. de SOUZA, Y.D. KIM, D.R. BOWMAN,  
N. CARLIN, C.K. GELBKE, W.G. GONG, W.G. LYNCH,  
L. PHAIR, and F. ZHU



*"Reaction plane determination for  $^{36}\text{Ar}+^{197}\text{Au}$  collisions at  $E/A=36$  MeV"*

**M. B. Tsang, R. T. de Souza, Y. D. Kim, D. R. Bowman, N. Carlin<sup>†</sup>, C. K. Gelbke,  
N. G. Gong, W. G. Lynch, L. Phair, and F. Zhu**

National Superconducting Cyclotron Laboratory  
and Department of Physics and Astronomy  
Michigan State University, East Lansing, MI. 48824, USA

Abstract: Collisions between  $^{36}\text{Ar}$  projectile and  $^{197}\text{Au}$  target nuclei at  $E/A=35$  MeV have been studied with the MSU Miniball, a  $4\pi$  phoswich array with a low detection threshold. Azimuthal distributions of light charged particles and intermediate mass fragments are extracted with respect to reaction planes determined from fission fragments or from the emission patterns of coincident light particles and intermediate mass fragments. The internal consistency and sensitivity to particle detection thresholds are explored for the various techniques of reaction plane determination. For the present reaction, the reaction plane can be determined with comparable accuracy from the distribution of fission fragments as from the orientation of the major axis of the transverse momentum tensor constructed from the emitted light particles and intermediate mass fragments. Monte Carlo calculations are performed which illustrate the sensitivity of the transverse momentum tensor method to the azimuthal anisotropy of the single particle distributions and the convergence of this method as a function of particle multiplicity. The extraction of experimental uncertainties in the determination of the reaction plane is discussed.

PACS Index: 25.70.Np

### *I. Introduction*

Microscopic descriptions of intermediate energy nucleus-nucleus collisions must account for the interplay between mean-field and nucleon-nucleon collision dynamics [1-21]. However, this interplay is sensitive to model parameters, such as the nuclear equation of state and the in-medium nucleon-nucleon cross section which are not yet accurately known. These quantities must, therefore, be determined from experimental data.

Calculations indicate that many promising observables are influenced strongly by the impact parameter and the orientation of the reaction plane, defined as the plane containing the relative momentum and position vectors of target and projectile nuclei [13,14,18,21]. Such dependences are difficult to observe in inclusive experiments which average over impact parameter and reaction plane orientation. More exclusive quantities, such as the emitted particle distributions for narrow ranges of impact parameter and well defined orientation of the initial collision plane ("triple differential cross sections"), are predicted to be much more sensitive to the in-medium nucleon-nucleon cross section and the nuclear equation of state than the single particle inclusive cross sections [14]. Similarly, more complex observables, such as collective flow [22-32], require the determination of impact parameter and orientation of the reaction plane. It is, therefore, important to optimize and understand the accuracy with which the reaction plane can be reconstructed from experimental data and to understand the intrinsic limitations of each method for reaction plane reconstruction.

At higher energies,  $E/A \gtrsim 100$  MeV, information about the magnitude of the impact parameter is traditionally obtained from the measured charged particle multiplicity [18,33-35]. At lower energies,  $E/A \approx 20-50$  MeV, comparable information on impact parameter has been extracted from measurements of the linear momentum transfer to fusion-like residues [36-38], charged particle [38,39] or neutron [40,41] multiplicities.

Information about the orientation of the reaction plane can be derived from the azimuthal anisotropies of the emitted particles. Such anisotropies may occur at higher energies,  $E/A \gtrsim 100$  MeV, due to sideward flow of nuclear

matter caused by compressional effects [22,23]. At lower energies,  $E/A \lesssim 100$  MeV, azimuthal anisotropies can result from a collective deflection of light particles to negative angles caused by the attractive nuclear mean field [42-49]. Information about the orientation of the reaction plane may be obtained by diagonalizing the transverse momentum tensor [42,43]. The reaction plane is then given by the plane spanned by the beam axis and the major axis of this tensor.

In studies of intermediate energy nucleus-nucleus collisions ( $E/A \lesssim 100$  MeV), diagonalization of the transverse momentum tensor was first used by Wilson et al. [42,43] for the analysis of near-symmetric collisions between relatively light nuclei ( $A \approx 40$ ). In these measurements, light particles were detected in  $4\pi$ -geometry with energy thresholds well above the exit channel Coulomb barrier. The effect of such thresholds on the accuracy of reaction plane determinations is not obvious. On the one hand, the azimuthal anisotropies of emitted particles increase strongly with the kinetic energy of the emitted particles [42-49], and it is not clear that the inclusion of low energy particles will improve the accuracy of the reaction plane determination. On the other hand, an improvement in accuracy of reaction plane determinations might nevertheless be obtained from the increase in statistical accuracy resulting from the larger numbers of detected particles and from the inclusion of intermediate mass fragments (IMFs) or fission fragments into the analysis. These latter reaction products are known [44,48-50] to exhibit particularly strong azimuthal anisotropies.

In this paper, we compare different techniques which can be employed for the determination of the reaction plane on an event-by-event basis. For this purpose, we performed measurements for the asymmetric reaction  $^{36}\text{Ar} + ^{197}\text{Au}$  at  $E/A = 35$  MeV using the MSU Miniball [51], a new low-threshold  $4\pi$  charged-particle detection array. For this reaction, the decay of heavy reaction residues by fission and/or emission of intermediate mass fragments occur with high probability. Thus it will be possible to compare the accuracy with which the orientation of the reaction plane can be determined from the distribution of emitted light particles or coincident fission fragments. In addition, it will be possible to assess the effects of particle detection thresholds.

This paper is organized as follows. Experimental details are given in Section II. In Section III, we define the methods which will be employed to extract the orientation of the reaction plane. Representative energy spectra and multiplicity distributions are presented in Section IV. In Section V, experimentally extracted azimuthal anisotropies with respect to the reaction plane will be presented and various methods will be compared. Section VI presents numerical simulations which serve to illustrate the accuracy with which the reaction plane can be reconstructed for events with different multiplicity. The influence of unknown weight functions is explored and the extraction of experimental uncertainties of reaction plane reconstructions is discussed. A summary will be given in Section VII.

## *II. Experimental Details*

The experiment was performed at the National Superconducting Cyclotron Laboratory of Michigan State University. An  $^{36}\text{Ar}$  beam of energy  $E/A=35$  MeV and intensity  $I \approx 10^8$  particles per second was extracted from the K500 cyclotron and transported to the 92" scattering chamber which housed the MSU Miniball phoswich detector array [51]. The areal density of the gold target was  $1 \text{ mg/cm}^2$ . During the experiment, a vacuum of better than  $10^{-5}$  torr was maintained in the scattering chamber. Water and hydrocarbon vapor components in the residual gas were strongly reduced by a large cold trap filled with liquid nitrogen. By this means, carbon deposits on the target were reduced to a negligible level.

Light particles and complex fragments were detected using rings 2-11 of the MSU Miniball phoswich detector array [51]. In this configuration, the array covered scattering angles of  $\theta_{\text{lab}}=16^\circ-160^\circ$  and a solid angle corresponding to 85% of  $4\pi$ . In Table 1, we list the solid angles and the ranges of polar and azimuthal angles which are covered by individual detectors of the Miniball. Additional details about the geometrical shapes of the detectors are given in ref. [51]. Each phoswich detector consisted of a  $40\mu\text{m}$  ( $4 \text{ mg/cm}^2$ ) thick plastic scintillator foil backed by a 2 cm thick CsI(Tl) crystal. The scintillation light was read out by photomultiplier tubes. All detectors had aluminized mylar foils ( $0.15 \text{ mg/cm}^2$  mylar and  $0.02 \text{ mg/cm}^2$  aluminum) placed in front of the plastic scintillator foils. As a precaution against secondary electrons, rings 2 and 3 were covered by aluminum foils of  $0.81 \text{ mg/cm}^2$  areal density. The

detector array was actively cooled and its temperature was stabilized. Gain drifts of the photomultiplier tubes were monitored by a light pulser system [51].

The anode currents from the photomultipliers were split and read out by three different FERA-ADCs gated over the time intervals  $\Delta t_{\text{fast}}=0-30$  ns,  $\Delta t_{\text{slow}}=100-500$  ns, and  $\Delta t_{\text{tail}}=1.0-2.4$   $\mu$ s, where  $t=0$  is defined as the leading edge of a given detector signal. In addition, the relative times of all discriminator signals were recorded. More details about the electronics and data acquisition system can be found in ref. [51]. Particles punching through the 4 mg/cm<sup>2</sup> plastic scintillator foils were identified by atomic number up to  $Z=18$  and by mass number, as well, for H and He isotopes. The approximate energy thresholds are  $E_{\text{th}}/A \approx 2$  MeV for  $Z=3$ ,  $E_{\text{th}}/A \approx 3$  MeV for  $Z=10$ , and  $E_{\text{th}}/A \approx 4$  MeV for  $Z=18$  fragments. Particles of lower energy which were stopped in the scintillator foils were recorded but could not be identified by atomic number.

All events in which at least two detectors fired were recorded on magnetic tape and analyzed off line. Random coincidences were negligible due to the low beam intensity.

Energy calibrations, accurate to within 5% were obtained by measuring the elastic scattering of <sup>4</sup>He, <sup>6</sup>Li, <sup>10</sup>B, <sup>12</sup>C, <sup>16</sup>O and <sup>35</sup>Cl beams from a <sup>197</sup>Au target at incident energies of  $E(^4\text{He})/A = 4.5, 9.4, 12.9, 16,$  and  $20$  MeV;  $E(^6\text{Li})/A = 8.9$  MeV;  $E(^{10}\text{B})/A = 15$  MeV;  $E(^{12}\text{C})/A = 6, 8, 13,$  and  $20$  MeV;  $E(^{16}\text{O})/A = 6, 8, 16,$  and  $20$  MeV; and  $E(^{35}\text{Cl})/A = 8.8, 12.3,$  and  $15$  MeV.

### *III. Definition of reaction planes*

In this section, we describe various methods for extracting the orientation of the reaction plane on an event-by-event basis. In Subsection A, we describe the extraction of the reaction plane from fission-like events detected in the Miniball. In Subsections B and C, we describe several procedures for determining the reaction plane from the distributions of light particles and intermediate mass fragments emitted in a given event. Throughout this paper, the "trigger" particle was eliminated from the algorithm used for the determination of the reaction plane to avoid self-correlations.

Corrections for recoil effects were taken into account when the reaction plane was determined from the distribution of coincident light particles and intermediate mass fragments.

### A. Fission Plane

The Miniball was originally designed as a low-threshold device for the detection of intermediate mass fragments. Unit elemental identification was obtained for particles with  $Z=1-18$  that punched through the plastic scintillators. It was also possible to discriminate lower-energy heavy fragments that stopped in the fast plastic scintillators from light particles. Indeed, from the measured pulse height in the fast gate, the corresponding time information, and the absence of signals in the slow and tail gates, it was possible to select low-energy heavy fragments which could result from fission. Even though the detection efficiency for fission fragments was not unity, significant numbers of events containing two fission-like fragments were observed. The association of such events with fission or fission-like processes is corroborated by the measured azimuthal correlation between coincident low-energy heavy fragments detected in rings 4-7, 9, and 10. (Ring 8, at  $\theta_{lab}=90^\circ$ , was not used for the identification of fission-like events since low-energy heavy particles emitted at  $\theta_{lab}=90^\circ$  are largely stopped in the target which was oriented normal to the beam axis.)

Figure 1 shows the distribution of relative azimuthal angles,  $\Delta\phi_{ff}$ , between coincident low-energy heavy fragments. These angles were defined over the angular interval of  $\Delta\phi_{ff}=0^\circ-180^\circ$  via the relation:  $\Delta\phi_{ff} = \cos^{-1} [\cos\phi_{f1}\cos\phi_{f2} + \sin\phi_{f1}\sin\phi_{f2}]$ , where  $\phi_{f1}$  and  $\phi_{f2}$  denote the azimuthal angles of the two fragments. As expected for fission, the azimuthal correlation is strongly peaked at  $\Delta\phi_{ff}=180^\circ$ , see solid line. The width of the distribution is due to smearing of the angular correlation by pre- and post-fission particle emission and by the finite granularity of the Miniball. The peak at  $\Delta\phi_{ff}\approx 180^\circ$  is broadened and shifted to smaller angles when energetic particles are emitted normal to the fission plane. This effect is illustrated by the dashed, dot-dashed, and dotted lines in Fig. 1 which show the azimuthal correlations of low-energy heavy fragments detected in coincidence with particles emitted with large momentum components normal to the fission plane. In our analysis,

two coincident low-energy heavy fragments were associated with fission when they satisfied the condition  $\Delta\phi_{ff} = 95^\circ - 180^\circ$ . For such events, we defined the orientation of the fission plane as:

$$\bar{\Phi}_F = \frac{1}{2} (\phi_{f1} + \phi_{f2} + 180^\circ) \quad , \text{ modulo } 180^\circ . \quad (1)$$

While the conservatively wide cut on  $\Delta\phi_{ff}$  reduces the loss of efficiency for reactions in which particles are emitted with large momentum components normal to the fission plane, it also causes some loss of resolution in the determination of the fission plane due to an increased background of particles not resulting from fission. Thus the present results can be improved by employing detectors capable of better discrimination between low-energy intermediate mass fragments and fission fragments.

### B. Gaussian Distributions of $\sin\phi$

Collective rotations or the deflection of particles in the mean field may lead to a hindrance of emission in a direction perpendicular to the reaction plane [44-49]. As a most simple ansatz, one may assume Gaussian distributions of the form

$$P(\phi - \bar{\Phi}; \vec{p}) \propto \exp[-\omega^2(E, M, \theta) \sin^2(\phi - \bar{\Phi})] \quad , \quad (2)$$

where  $\bar{\Phi}$  denotes the azimuthal angle of the reaction plane and  $\phi$  is the azimuthal angle of the emitted particle. The weight function  $\omega(E, M, \theta)$  can depend on the particle's energy  $E$ , mass  $M$ , and polar angle  $\theta$  with respect to the beam axis. For simplicity, we do not carry explicitly the additional dependence on the magnitude of the impact parameter of the collision. Distributions similar to Eq. 2 also describe the shapes of azimuthal distributions for fission of rapidly rotating fusion residues [44].

In the following, we assume that individual emissions are uncorrelated, i.e. we neglect many-particle correlations. Under this assumption, the joint probability for emitting  $N$  particles in a particular event can be written as:



$$P(\bar{\alpha}; \vec{p}_1, \dots, \vec{p}_N) \propto \exp\left[\sum_{i=1}^N -\omega_i^2(E_i, M_i, \theta_i) \sin^2(\phi_i - \bar{\alpha})\right]. \quad (3)$$

In a typical nuclear collision experiment, the orientation of the reaction plane is unknown, and one can try to reconstruct it from the measured distribution of emitted particles. When  $N$  particles are detected in a given event, the most probable orientation of the reaction plane corresponds to the maximum of the joint probability. The necessary condition

$$\frac{d}{d\bar{\alpha}} P(\bar{\alpha}; \vec{p}_1, \dots, \vec{p}_N) = 0 \quad (4)$$

can be cast into the form:

$$\text{tg}(2\bar{\alpha}) = \frac{\sum_{i=1}^N \omega_i^2(E_i, M_i, \theta_i) \sin 2\phi_i}{\sum_{i=1}^N \omega_i^2(E_i, M_i, \theta_i) \cos 2\phi_i}. \quad (5)$$

Over the angular interval of  $\bar{\alpha} = 0^\circ - 180^\circ$ , this equation has two solutions,  $\bar{\alpha}_1$  and  $\bar{\alpha}_2$ , which differ by  $90^\circ$ . These two solutions give the maximum and minimum of the sum

$$\Sigma(\bar{\alpha}) = \sum_{i=1}^N \omega_i^2(E_i, M_i, \theta_i) \sin^2(\phi_i - \bar{\alpha}). \quad (6)$$

The value of  $\bar{\alpha}$  which gives the minimum corresponds to the most probable orientation of the reaction plane. It is straightforward to show that the two solutions of Eq. 5 define the directions of the principal axes of a tensor,

$$\Omega_{nm} = \sum_i (\omega_{in} \omega_{im}), \quad (7)$$

where  $i$  is the particle index, and  $n$  and  $m$  label the components of the two-dimensional vector

$$(\omega_{i1}, \omega_{i2}) = [\omega(E_i, M_i, \theta_i) \cos \phi_i, \omega(E_i, M_i, \theta_i) \sin \phi_i]. \quad (8)$$

The maximum and minimum values of the sum in Eq. 6 are equal to the lengths of the major and minor axes of the tensor  $\Omega_{nm}$ .

For illustration, Fig. 2 shows a few representative examples of the family of curves represented by Eq. 2 (for  $\Xi=0^\circ$ ). For ease of representation, we have normalized all curves to  $P(0^\circ)=1$ . One may characterize these and similar distributions by the variance,

$$\langle \phi^2 \rangle^{1/2} = \left( \frac{\int \phi^2 P(\phi) d\phi}{\int P(\phi) d\phi} \right)^{1/2}, \quad (9)$$

or the azimuthal asymmetry coefficient,

$$A_\phi = P(0^\circ)/P(90^\circ) = \exp[\omega^2(E, M, \theta)]. \quad (10)$$

For orientation, the relation between  $\omega$ ,  $\langle \phi^2 \rangle^{1/2}$ , and  $A_\phi$  is depicted in Fig. 3.

While parametrizations of the form of Eq. 2 are reasonable, they are by no means unique. Nevertheless, azimuthal anisotropy coefficients and variances of experimental azimuthal distributions are useful parameters for their characterization. For broad probability distributions, the azimuthal anisotropy coefficient is a useful and sensitive parameter. For narrow distributions, the variance appears more appropriate since the azimuthal anisotropy coefficient becomes overly sensitive to the functional form with which the tail of the distribution is described.

As a most simple ansatz, one may assume that the weight function  $\omega(E, M, \theta)$  is linearly dependent on the transverse momentum of the emitted particles,

$$\omega(E, M, \theta) = \epsilon \sin\theta \sqrt{2ME} = \epsilon p \sin\theta. \quad (11)$$

Here,  $\epsilon$  is a proportionality constant. For  $\epsilon=0$  the azimuthal distributions are isotropic; for  $\epsilon>0$  the azimuthal distributions are enhanced in the reaction plane. Qualitatively, such an ansatz accounts for the experimental observation

that azimuthal anisotropies increase with mass and energy of the emitted particles and that they are most pronounced at angles close to  $\theta=90^\circ$  [42-50]. With this ansatz, the orientation of the reaction plane is determined by solving the equation

$$\text{tg}(2\bar{\Phi}) = \frac{\sum_{i=1}^N p_i^2 \sin^2 \theta_i \sin 2\phi_i}{\sum_{i=1}^N p_i^2 \sin^2 \theta_i \cos 2\phi_i}, \quad (12)$$

and using that solution which gives the minimum of the sum:

$$\Sigma_p(\bar{\Phi}) = \sum_{i=1}^N p_i^2 \sin^2 \theta_i \sin^2(\phi_i - \bar{\Phi}). \quad (13)$$

Equations 12 and 13 are mathematically equivalent to the method used by Wilson et al. [42,43] who proposed to reconstruct the orientation of the reaction plane by minimizing the sum of the squares of the momentum components perpendicular to the reaction plane, Eq. 13. This method was applied to the analysis of azimuthal distributions for near-symmetric collisions at intermediate energies [42,43]. Equation 12 is also mathematically equivalent to the diagonalization of the transverse momentum tensor,  $A_{nm} = \sum_i (p_{in} p_{im})$ , where  $\vec{p}_i = (p_{i1}, p_{i2}) = (p_i \sin \theta_i \cos \phi_i, p_i \sin \theta_i \sin \phi_i)$  is the transverse momentum of particle  $i$ .

### C. Rotating Hot Gas

In order to explore whether reaction plane determinations based upon Eq. 12 are sensitive to the functional form of the azimuthal distributions, we have employed an alternative parametrization of the azimuthal emission probability which is related to the energy and angular distributions for particles emitted from a hot gas rotating about an axis perpendicular to the reaction plane and moving with a velocity  $\vec{v}$  parallel to the beam axis [46].

A simple expression can be obtained by neglecting Coulomb effects and writing Eq. 5 of ref. [46] in a slightly different form:

$$P(\Phi; \vec{p}) \propto p_s \exp(-p_s^2/2MT) \left[ \frac{J_1(K)}{K} \right] . \quad (14)$$

Here,  $J_1$  denotes the first-order Bessel function, and

$$K = \frac{R\omega}{T} [p_s^2 - p^2 \sin^2 \theta \sin^2(\Phi - \Xi)]^{1/2} . \quad (15)$$

The momentum in the rest frame of the emitting source is given by

$$p_s^2 = p^2 + m^2 v^2 - 2m\bar{v}p \cos \theta . \quad (16)$$

If one neglects non-exponential factors and factors which are independent of azimuthal angle, one can approximate  $J_1(K)/K$  as proportional to  $\exp(K)$  and make the ansatz:

$$P(\Xi; \vec{p}) \propto \exp[k(p_s^2 - p^2 \sin^2 \theta \sin^2(\Phi - \Xi))^{1/2}] , \quad (17)$$

where  $k=R\omega/T$  is considered as an unknown width parameter. The orientation of the reaction plane can then be extracted by maximizing the joint probability,

$$P(\Xi; \vec{p}_1, \dots, \vec{p}_N) \propto \exp[k \sum_{i=1}^N (p_{s_i}^2 - p_i^2 \sin^2 \theta_i \sin^2(\Phi_i - \Xi))^{1/2}] . \quad (18)$$

This maximum can be determined numerically by finding the maximum of the sum term in the exponent or by solving the equation for  $dP/d\Xi=0$ .

#### IV. Energy Spectra and Multiplicity Distributions

For reference, Fig. 4 presents the energy spectra of light particles detected at  $\theta_{lab}=45^\circ$ . At this angle, particle emission is dominated by non-compound emission processes. While the low energy portions of the spectra are likely to contain contributions from the decay of equilibrated heavy reaction residues, contributions from quasi-elastic projectile breakup reactions are of minor importance. Particles emitted at this angle were chosen as "trigger particles" for the analysis of azimuthal distributions with respect to the reaction plane since (i) the azimuthal distributions at this angle are known [49] to exhibit large anisotropies and (ii) the yields of intermediate mass

fragments emitted at this angle are sufficiently large to allow an analysis of their azimuthal distributions.

Transverse energy distributions,  $E_t = E \sin^2 \theta$ , for protons, deuterons, tritons, and  $\alpha$ -particles are shown in Fig. 5. The distributions shown in the figure were obtained by integration over all detector rings. The solid lines in the figure represent simple exponential probability distributions of the form

$$P(E_t) \propto \exp(-E_t/T_i), \quad (19)$$

characterized by temperature parameters  $T_i$  indicated in the figure and also listed in Table 2. Transverse energy distributions approximated by Eq. 19 will be used in the Monte-Carlo simulations discussed in Section VI.

Figure 6 presents a two-dimensional contour diagram of the relative probability to detect a total of  $N_C$  identified charged particles with  $N_{IMF}$  identified intermediate mass fragments (IMFs) among them. Over a rather broad range of particle multiplicities, the average number of detected intermediate mass fragments is of the order of unity.

Figure 7 presents experimental multiplicity distributions for the emission of charged particles [ $P(N_C)$ , left hand panel] and intermediate mass fragments [ $P(dN_{IMF})$ , right hand panel]. The solid points represent inclusive distributions, and the open points correspond to distributions detected in coincidence with two fission fragments selected, as before, by the requirement  $\Delta\phi_{ff} = 95^\circ - 180^\circ$ . The selection of events with two fission fragments in the exit channel, leads to a slight suppression of reactions with high charged particle and IMF multiplicities. Nevertheless, the two distributions are rather similar, indicating that the requirement of two fission fragments in the exit channel imposes only a relatively modest bias on impact parameter selection.

#### V. Comparison of Different Methods

In this section we compare various methods which can be employed to tag the orientation of the reaction plane. In Subsection A, we compare azimuthal

distributions determined by using Eqs. 1 and 12. Recoil effects are discussed in Subsection B. In Subsection C, we discuss angular differences between reaction planes determined by the various methods. A quantitative comparison of azimuthal anisotropy coefficients and variances extracted by means of the fission and transverse momentum tensor techniques is given in Subsection D; dependences on particle type and energy are explored. In Subsection E, we discuss the influence of detection thresholds on the accuracy of reaction plane determinations based upon Eq. 12. Unless otherwise stated, all comparisons utilize the same set of data, pre-selected by the requirement that two fission fragments were detected and that, in addition, the combined number of identified light particles and intermediate mass fragments was  $N=4-9$ . Higher multiplicities were excluded in this analysis since they select more central collisions for which the azimuthal distributions are reduced [52].

#### *A. Azimuthal distributions*

Azimuthal distributions of light particles and intermediate mass fragments are shown in Fig. 8. Different panels of the figure show the azimuthal distribution of the indicated "trigger particle" with respect to the orientation of the reaction plane reconstructed from the remaining detected particles. The distributions were normalized to an average value of unity. An energy gate of  $E/A=12-20$  MeV was applied to the trigger particles, energy thresholds for all other particles were set as discussed in Section II. Open points show azimuthal distributions measured with respect to the fission plane, Eq. 1. Solid points show azimuthal distributions measured with respect to the plane determined with the transverse momentum tensor method [42,43], Eq. 12. Quantitatively consistent azimuthal distributions are extracted from both methods, revealing enhanced emission in the reaction plane.

In order to display similarities and differences between various methods in a more compact form, we define the experimental azimuthal anisotropy coefficient  $A_\phi$  as the ratio of in-plane and out-of-plane yields,

$$A_\phi = \frac{2Y(\Delta\phi=0^\circ-10^\circ)}{Y(\Delta\phi=70^\circ-90^\circ)} \quad (20)$$

In this definition, statistical errors are reduced by integrating out-of-plane yields over angular intervals twice as large as for in-plane yields. For strongly focussed azimuthal distributions, the azimuthal anisotropy coefficient can be rather sensitive to resolution effects at  $\Delta\phi=0^\circ$  and  $\Delta\phi=90^\circ$ . Such effects may be less relevant for some applications. Therefore, we also extract the variance,  $\langle\phi^2\rangle^{1/2}$ , of the experimental azimuthal distribution, see Eq. 9. The variance of an isotropic distribution is  $52^\circ$ .

### B. Correction for Recoil Effects

Determinations of the reaction plane may suffer from self-correlations due to momentum conservation [23,30], as the detection of a trigger particle with large transverse momentum requires a corresponding opposing transverse momentum for the remaining system. Distortions of angular correlations from momentum conservation effects are particularly pronounced for light systems [30,45,46,53,54]. Since it is unknown how the recoil momentum imposed by the trigger particle is distributed among the remaining particles, corrections for such distortions are model dependent.

We have assessed the effects of momentum conservation by employing the technique proposed by ref. [30]. In this approach, one assumes that the transverse momentum,  $\vec{p}_t$ , of the trigger particle is balanced by a coherently recoiling source of mass  $M_S$ . Particles of mass  $m_i$  emitted from this recoiling source carry an additional transverse recoil momentum,  $\Delta\vec{p}_{t,i} = -\vec{p}_t m_i/M_S$ . From the measured transverse momenta,  $\vec{p}_{t,i}$ , of the coincident particles one constructs recoil-corrected transverse momenta,  $\vec{p}'_{t,i}$ , according to the prescription

$$\vec{p}'_{t,i} = \vec{p}_{t,i} + \vec{p}_t m_i/M_S. \quad (21)$$

The orientation of the reaction plane is determined from these corrected transverse momenta. The number of nucleons in the recoiling source must be considered as an undetermined parameter, since it is not clear which particles share the recoil momentum imparted by the trigger particle. If the entire residual system recoils collectively, one would choose  $M_S = M_{res}$  [30] where  $M_{res}$  is the total mass of the residual system. Such an assumption would be well

justified for the sequential decay of compound nuclei. However, for non-compound emission processes, the situation is less well defined. An alternative, extreme assumption would be  $M_S = 2m_0 Z_C$ , where  $m_0$  is the nucleon mass and  $Z_C$  is the total charge of detected light particles and intermediate mass fragments. Such a choice could be reasonable if one assumed that all detected particles were emitted from a clean-cut participant region, containing equal numbers of protons and neutrons, which did not interact with the spectator nuclei. The actual recoil effects are likely to lie within these extremes. More accurate evaluations of recoil effects require complete dynamical treatments of the reaction.

In order to assess the importance of recoil effects in more general terms, we have considered the mass,  $M_S$ , of the coherently recoiling source as an undetermined parameter and explored the sensitivity of the azimuthal asymmetry coefficient to this parameter for lithium fragments of energies  $E/A \geq 8$  MeV upon this parameter. The results are shown in Fig. 9. For  $M_S > 40m_0$ , the extracted azimuthal anisotropy depends only weakly on  $M_S$ ; however, for smaller values,  $A_\phi$  rises strongly as a function of  $M_S$ . Most likely such a strong dependence arises from an over-correction of the recoil effect. In any case, such small values are difficult to justify for collisions excluding the most peripheral interactions, and the resulting large corrections must be viewed as unreliable. For the remainder of our analysis, we chose  $M_S = 72m_0$ , corresponding to a coherently recoiling source consisting of twice the number of projectile nucleons. Our final results and conclusions are rather insensitive to the applied recoil correction.

### *C. Differences Between Reaction Plane Orientations*

It is important to know whether different techniques determine similar planes. Figure 10 shows distributions,  $P(\Delta\Phi)$ , of relative orientations between planes extracted by different methods. Since no polarizations are determined, the angle between any two planes can only be defined between  $\Delta\Phi = 0^\circ$  and  $\Delta\Phi = 90^\circ$ . For convenience of comparison, we have adopted the normalization  $P(\Delta\Phi = 0^\circ) = 1$ . For compactness of notation,  $\Phi_F$  denotes the azimuthal orientation of the fission plane determined from Eq. 1;  $\Phi_{PT}$  and  $\Phi_{rot}$  denote the azimuthal



orientations of planes extracted from Eqs. 12 and 18, respectively. The orientation of these latter planes were extracted from the distributions of identified light particles and intermediate mass fragments.

The solid line in Fig. 10 shows the difference between  $\bar{\alpha}_{PT}$  and  $\bar{\alpha}_{rot}$ . Clearly, these two planes are virtually identical. In view of the simple form of Eq. 12, the use of this (or a mathematically equivalent equation [42,43]) appears more convenient and preferable.

Relatively large differences exist between the orientation of the fission plane and the plane defined by the orientation of the major axis of the transverse momentum tensor constructed from the distribution of light particles and intermediate mass fragments. These differences are shown by the solid points in Fig. 10. Nevertheless, the most probable relative orientation between the fission plane and planes extracted from the distribution of associated particles is  $\Delta\bar{\alpha}=0^\circ$ .

The rather broad distribution of  $|\bar{\alpha}_F - \bar{\alpha}_{PT}|$  reflects limitations of the transverse momentum tensor and/or fission methods for average types of events. For example, the distribution becomes narrower when one selects events with at least one energetic ( $E > 80$  MeV)  $\alpha$ -particle detected in rings 4-7, see open points in Fig. 10. Intrinsic uncertainties of the two methods will be discussed in Section VI.

#### *D. Azimuthal Anisotropies*

Figures 11 and 12 show azimuthal anisotropy coefficients and variances of azimuthal distributions measured with respect to reaction planes determined with Eq. 12 from the light-particle and IMF emission patterns (open points) or, alternatively, with Eq. 1 from fission fragments (solid points). In all cases, the trigger particles were detected at  $\theta=45^\circ$ . Different panels show results for different ranges of kinetic energy per nucleon of the trigger particle. Consistent with previous observations [44-50], the azimuthal anisotropies increase with mass and kinetic energy of the detected trigger particle. In all cases, the azimuthal anisotropy coefficients extracted with the fission and transverse momentum tensor techniques are very similar.

We have explored the possibility of determining the reaction plane with improved resolution by including all detected (but not identified) low-energy heavy fragments into the analysis. For this purpose, low energy fragments stopped in the fast plastic scintillator foils were given the weight of fast  $\alpha$ -particles with a transverse momentum of

$$p_f = 1.1 \sin^2 \theta \text{ GeV}/c . \quad (22)$$

Our final conclusions are not very sensitive to this specific choice, and qualitatively similar results are obtained for slightly different weights. Azimuthal anisotropy coefficients and variances extracted by diagonalizing the momentum tensor for all detected particles (Eqs. 12, 22) are shown by the open squares in Figs. 11 and 12, respectively. With this combined technique, slightly larger azimuthal anisotropy coefficients are extracted for heavy and energetic particles than were obtained with either the fission technique or the transverse momentum tensor technique alone, pointing towards intrinsic limitations of both techniques.

Similar improvements are also obtained when one analyzes data preselected by the condition that at least one low-energy heavy fragment was detected, irrespective whether it is detected in coincidence with a second fragment or with several fragments. These results are shown in Fig. 13. The open squares and solid points show anisotropy coefficients extracted by the transverse momentum method including and excluding, respectively, unidentified low-energy heavy fragments into the analysis by means of Eq. 22. These results suggest that significant improvements in resolution could be obtained with detectors capable of identifying heavier particles and with lower energy thresholds than was possible in the present experiment. However, the true improvement may be less than suggested by the Fig. 13, since we could not apply reliable corrections for recoil effects to unidentified low-energy heavy fragments.

#### *E. Effects of Detection Thresholds*

For increasingly violent heavy ion collisions, fast particle emission leads to heavy residues of decreasing fissility. Thus, the likelihood for fission in the exit channel decreases. Indeed, for nucleus-nucleus collisions at

relativistic energies, fission is only observed for peripheral collisions [55-57]. For collisions at smaller impact parameters, the orientation with respect to the reaction plane must then be inferred from the light particle and intermediate mass fragment emission patterns.

Optimum determinations of the reaction plane are expected when large numbers of energetic  $\alpha$ -particles or intermediate mass fragments are detected in the exit channel. For a given class of collisions, one might hope to improve the determination of the reaction plane by raising the particle detection threshold in an attempt to reduce the "noise" from randomly emitted particles which bear little memory of the reaction plane. On the other hand, low-energy particles might still retain some limited memory of the reaction plane and their inclusion might help improve the statistical accuracy of reaction-plane determinations on an event-by-event basis. At present, microscopic calculations predict the emission of low-energy particles with limited accuracy only. Therefore, the relative advantages of including or excluding low-energy particles are best evaluated with real data.

In Fig. 14, we demonstrate the influence of particle detection thresholds on the magnitude of the azimuthal anisotropy coefficients for reaction plane reconstructions based upon Eq. 12. The data set used in this analysis was preselected by the requirement  $N=4-9$  and the reaction plane was determined from the subset of light particles and intermediate mass fragments which satisfied the indicated threshold requirements. Thus the bias on impact parameter selection was kept constant, while the number of particles included in the determination of the reaction plane depended on the indicated energy threshold. The results are clear: For the present reaction, the inclusion of low-energy particles and intermediate mass fragments improves the definition of the reaction plane.

## *VI. Monte-Carlo Simulations*

In this section, we explore the convergence of the transverse momentum tensor method by performing Monte Carlo calculations. In Subsection A, we investigate improvements in accuracy as a function of particle multiplicity and

average azimuthal anisotropy of the emitted particles. In Subsection B, we explore the sensitivity to optimum choices of the weight functions used in Eq. 5. In Subsection C, we discuss the determination of the experimental uncertainties of reaction plane determinations.

#### A. Dependence on Azimuthal Anisotropy and Multiplicity

The accuracy with which the reaction plane can be determined from the distribution of light particles depends both on the charged particle multiplicity and on the anisotropy coefficient  $A_\phi$  characterizing the azimuthal distributions of the emitted particles. In order to explore the degree of accuracy with which the reaction plane can be reconstructed from the measured particle distributions, we have performed Monte-Carlo simulations which generate events of fixed multiplicity with particles distributed azimuthally according to Eq. 2. In this and the following calculations, we assumed stochastic emission of light particles of mass  $A=1-4$  with relative weights  $\sigma_i$  ( $i=1-4$ ) taken from the p, d, t, and  $\alpha$  cross sections measured for the present reaction. The probability distributions of the transverse energies,  $E_t = (p^2/2m)\sin^2\theta$ , were approximated by exponential functions, Eq. 19, characterized by temperature parameters  $T_i$  determined from the slopes of the angle integrated transverse energy distributions shown in Fig. 5. As a further simplification, we introduced sharp cuts in the range of transverse energies over which the emission of particles was simulated. The detailed parameters used in the simulations are listed in Table 2. For computational speed, the calculations were performed on a grid with binning widths  $\Delta\phi=1^\circ$  and  $\Delta E_t = \Delta E \sin^2\theta = 1$  MeV.

For each event, Eq. 5 was used to reconstruct the orientation of the reaction plane. For each ensemble of events, characterized by a given weight function and a fixed number of particles used for the reconstruction of the reaction plane, we calculated the probability distribution,  $P(\Delta\Phi)$ , of relative orientations between the "true" and reconstructed reaction planes. As before, we adopted the normalization  $P(\Delta\Phi=0^\circ)=1$ .

As a first instructive example, we performed calculations for the (unrealistic) case of constant weight functions,  $\omega(E, M, \theta) = \text{constant}$ , and studied the accuracy with which the reaction plane was reconstructed as a

function of particle multiplicity. The results of these schematic calculations are shown in Figs. 15 and 16. Figure 15 shows the azimuthal distributions of the reconstructed reaction planes. Different panels in the figures are labeled by the azimuthal anisotropy coefficients,  $A_\phi = \exp(\omega^2)$ , characterizing the single particle probability functions. The curves in each panel are labelled by the number,  $N$ , of particles used for the reconstruction of the reaction plane. (Trivially, curves for  $N=1$  are identical with the single particle distributions.) The calculations confirm the qualitative expectation that the orientation of the reaction plane can be reconstructed with improved accuracy when more particles are detected. In general, however, the convergence as a function of  $N$  is rather slow. The figure also illustrates that much can be gained, even at very low multiplicity, if one detects particles which have azimuthal distributions characterized by large azimuthal anisotropy coefficients  $A_\phi$ . The solid curves in Fig. 16 depict the rate of convergence in a more compact form. Here, the variances,  $\langle \Delta\Phi^2 \rangle^{1/2}$ , of the distributions  $P(\Delta\Phi)$  are shown as a function of particle number  $N$ . (Note that:  $\langle \Delta\Phi^2 \rangle^{1/2} \approx 52^\circ$  for isotropic distributions, see also Fig. 3.) The different curves are labelled by the azimuthal anisotropy coefficients characterizing the underlying single particle distributions.

In more realistic situations, the weight function depends on particle type and energy. In such cases, the convergence of reaction plane reconstructions as a function of particle multiplicity depends on the energy spectra, the relative weights of various detected particles, and on the functional form of the weight function. To illustrate this effect, we have performed calculations for weight functions of the form  $w = \epsilon \sin\theta$  for which the transverse momentum tensor method is optimal and Eqs. 5 and 12 are identical.

The dashed curves in Fig. 16 show that reaction plane reconstructions converge slightly more rapidly as a function of particle multiplicity when the weight function is proportional to the transverse momentum, Eq. 11, as compared to the less realistic case when it is constant (solid lines). Qualitatively, this more rapid convergence is related to our previous observation that much can be gained from particles with large transverse momenta for which  $A_\phi$  is large. A set of  $N>1$  particles is likely to contain some energetic

particles for which the azimuthal distribution is considerably more anisotropic than for the average particle set. Such energetic particles can tag the orientation of the reaction plane more accurately than several particles with average azimuthal anisotropies, provided the weights of these particles are properly taken into account.

### *B. Sensitivity to Optimum Choice of Weight Functions*

When the weight function  $\omega(E, M, \theta)$  is known, solutions of Eq. 5 provide the best estimate for the orientation of the reaction plane. However, in general, the weight function is not known, and one has to rely on empirical procedures. For intermediate energy heavy ion reactions, the diagonalization of the transverse momentum tensor, Eq. 12, has been used with good success [42,43]. It is, therefore, of interest to explore the convergence of this method for azimuthal distributions of the form of Eq. 2, but with weight functions different from Eq. 11, i.e for cases for which Eq. 12 does not present the best possible method.

Such comparisons are presented in Fig. 17. In these calculations, we have assumed azimuthal distributions given by Eq. 2 with  $\omega = \text{constant}$  (left hand panels) and  $\omega = \sqrt{\epsilon} \sin \theta$  (right hand panels). The dashed curves show the distributions  $P(\Delta\Phi)$  obtained by reconstructing the reaction plane with Eq. 12 and the solid curves show the distributions obtained by reconstructing the reaction plane with the optimum relation, Eq. 5. Trivially, the two curves coincide for  $N=1$ , giving the average single particle distribution. For larger multiplicities, the use of the optimum relation, Eq. 5, gives narrower distributions for  $P(\Delta\Phi)$ . While the differences for  $\omega = \text{constant}$  are still appreciable, they become insignificant for  $\omega = \sqrt{\epsilon} \sin \theta$ . Thus reconstructions of the reaction plane at low particle multiplicities are only moderately sensitive to the detailed functional form of the weight functions, as long as they account for the rough trends of azimuthal anisotropies as a function of particle type and momentum. This insensitivity to the detailed shape of the weight function also provides a qualitative understanding for the improvement which could be obtained by including particles which exhibit strongly

anisotropic azimuthal distributions, such as low-energy heavy fragments, even when their weight functions are not accurately known.

### C. Estimate of Experimental Uncertainties

Experimental uncertainties of reaction plane reconstructions can be estimated [22, 23] by randomly subdividing each event of multiplicity  $N$  into two subsets 1 and 2, each of multiplicity  $\frac{1}{2}N$ . For each subset, one determines the orientation of the reaction plane according to Eq. 5 and extracts the angle  $\Delta\Phi_{12}$  between these two planes. From the probability distribution  $P(\Delta\Phi_{12})$  one can make inferences about the accuracy with which the reaction plane can be reconstructed for the complete event.

The problem can be analyzed in two steps. First, the experimental distribution  $P(\Delta\Phi_{12})$  is used to make an estimate for the probability distribution  $P_{\frac{1}{2}N}(\Delta\Phi)$  of the angle between the true reaction plane and the reaction plane determined from  $\frac{1}{2}N$  particles. Second, one uses the distribution  $P_{\frac{1}{2}N}(\Delta\Phi)$  to make an estimate about the distribution  $P_N(\Delta\Phi)$  for events with  $N$  detected particles. In this step, one must estimate how the accuracy of the extraction of the reaction plane is improved by increasing the number of detected particles from  $\frac{1}{2}N$  to  $N$ . Numerical calculations, performed for single particle distributions of the form of Eq. 2, indicate that both steps can be made rather quantitatively and with little dependence on detailed model assumptions.

Figure 18 shows experimental distributions  $P(\Delta\Phi_{12})$  extracted from our data using Eq. 12. The left hand panel shows the distribution extracted from identified light particles and intermediate mass fragments and the right hand panel shows the distribution for which low energy heavy fragments were included according to the prescription of Eq. 22. The solid lines show the results of Monte-Carlo calculations for the distribution  $P(\Delta\Phi_{12})$  for events generated with multiplicity  $N=8$ , using weight functions  $w=\epsilon\psi\sin\theta$  (Eq. 11) and transverse energy distributions given by Eq. 19. In these calculations, the weight factors  $\epsilon$  were adjusted to reproduce the experimental distribution. The dot-dashed and dashed curves show the calculated distributions  $P_{\frac{1}{2}N}(\Delta\Phi)$  and  $P_N(\Delta\Phi)$  for the relative orientations between the true reaction plane and the

planes reconstructed from subset containing  $\frac{1}{2}N=4$  and from the full set containing  $N=8$  particles, respectively. Even though the distributions for  $P(\Delta\bar{\alpha}_{12})$  are broad, the predicted accuracy of the reaction plane determination for the full event is rather satisfactory, especially when low-energy heavy fragments are incorporated into the analysis. The rather large difference between the distributions  $P(\Delta\bar{\alpha}_{12})$  and  $P_{\frac{1}{2}N}(\Delta\bar{\alpha})$ , solid and dot-dashed curves, arises from the convolution of the probability distribution  $P_{\frac{1}{2}N}(\Delta\bar{\alpha})$  with itself:

$$P(\Delta\bar{\alpha}_{12}) = \int P_{\frac{1}{2}N}(\bar{\alpha})P_{\frac{1}{2}N}(\bar{\alpha}+\Delta\bar{\alpha}_{12})d\bar{\alpha} . \quad (23)$$

The difference between the distributions  $P_{\frac{1}{2}N}(\Delta\bar{\alpha})$  and  $P_N(\Delta\bar{\alpha})$  shown by the dot-dashed and dashed curves arises from the improvement in accuracy with a doubling of the multiplicity, see also Fig. 16.

The calculated probability distributions  $P(\Delta\bar{\alpha})$  for the angle between the true and reconstructed reaction planes are qualitatively similar in shape to the family of curves represented by Eq. 2, compare Figs. 2, 15 and 17. Therefore, one may hope to be able to relate the most important characteristics of the functions  $P(\Delta\bar{\alpha}_{12})$  and  $P_{\frac{1}{2}N}(\Delta\bar{\alpha})$  without much sensitivity to details of the weighting functions or particle multiplicities employed for the reconstruction of the reaction plane. In order to explore this possibility, we have performed a number of calculations with Eqs. 2, 11 and 12 using various parameters  $\varepsilon$  and different multiplicities. For each of the calculated distributions,  $P(\Delta\bar{\alpha}_{12})$  and  $P_{\frac{1}{2}N}(\Delta\bar{\alpha})$ , we have extracted the azimuthal anisotropies,  $A_{\bar{\alpha}_{12}}$  and  $A_{\bar{\alpha}_{\frac{1}{2}N}}$  (Eq. 10), and the variances,  $\langle \Delta\bar{\alpha}_{12}^2 \rangle^{1/2}$  and  $\langle \Delta\bar{\alpha}_{\frac{1}{2}N}^2 \rangle^{1/2}$  (Eq. 9). The relation between the calculated azimuthal anisotropy coefficients is shown by the open points in the bottom panel of Fig. 19; the points in the top panel show the relation between the variances. The calculated relation between these quantities follows rather closely the relation obtained by convoluting functions of the form of Eq. 2 (with  $\omega=\text{constant}$ ) in analogy to Eq. 23. This latter relation is shown by the solid curves in Fig. 19.

Reversing the argument, one may use the solid curves shown in Fig. 19 to assess the shape of the distribution  $P_{\frac{1}{2}N}(\Delta\bar{\alpha})$  from the measured distribution  $P(\Delta\bar{\alpha}_{12})$ . The results shown in Fig. 16 suggest that the extrapolation from



$P_{\frac{1}{2}N}(\Delta\Phi)$  to  $P_N(\Delta\Phi)$  may be somewhat uncertain if the exact shape of the weight function is not known. In order to assess such uncertainties, we have calculated the variances,  $\langle \Delta\Phi_{\frac{1}{2}N}^2 \rangle^{1/2}$  to  $\langle \Delta\Phi_N^2 \rangle^{1/2}$ , of distributions,  $P_{\frac{1}{2}N}(\Delta\Phi)$  and  $P_N(\Delta\Phi)$ , for a broad range of multiplicities and/or azimuthal anisotropy coefficients of the average single particle distributions. Examples of such calculations are shown by the open and solid points in Fig. 20. Open and solid points represent calculations with momentum dependent ( $\omega = \epsilon \sin\theta$ ) and momentum independent ( $\omega = \omega_0 = \text{const.}$ ) weight functions for various choices of the parameters  $\epsilon$  and  $\omega_0$ , respectively. The numerical simulations indicate that the dependence on the weight function is rather weak. Moreover, the variances of the two distributions are found to follow a nearly universal curve, independent of the value of  $N$ . (Trivially, for very large  $N$ , the central limit theorem predicts that the two distributions should be related by a factor of  $\sqrt{2}$ .) Hence, the extrapolation from  $\langle \Delta\Phi_{\frac{1}{2}N}^2 \rangle^{1/2}$  to  $\langle \Delta\Phi_N^2 \rangle^{1/2}$  is also rather model independent. For future reference, we have fit the points in Fig. 20 with a simple polynomial of the form:

$$\langle \Delta\Phi_N^2 \rangle^{1/2} = 2.292 + 0.276 \langle \Delta\Phi_{\frac{1}{2}N}^2 \rangle^{1/2} + 0.135 \langle \Delta\Phi_{\frac{1}{2}N}^2 \rangle \quad (24)$$

The arguments can be generalized to assess the relative accuracy of reaction plane determinations by the fission and transverse momentum tensor methods for events in which two fission fragments are detected in the exit channel. Figure 21 shows the distributions,  $P(\Delta\Phi)$ , for the relative orientations of planes determined from two half-subsets of light particles and IMFs [ $P(\Delta\Phi_{1-2})$ : solid points]; from one half-subset and from fission fragments [ $P(\Delta\Phi_{F-1})$ : star shaped points]; from fission fragments and from the full set of  $N=4-9$  light particles and IMFs [ $P(\Delta\Phi_{F-N})$ : open squares]. In order to obtain estimates of the primary distributions [ $P_{\frac{1}{2}N}(\Delta\Phi)$ ,  $P_N(\Delta\Phi)$ ,  $P_F(\Delta\Phi)$ ] of the experimentally determined planes with respect to the true reaction plane, we assume that the relative orientations between two planes A and B can be described by convolutions of the form

$$P(\Delta\Phi_{A-B}) = \int P_A(\Phi) P_B(\Phi + \Delta\Phi_{A-B}) d\Phi \quad (25)$$

where  $P_A(\Phi)$  and  $P_B(\Phi)$  denote the probability distributions for the angle  $\Phi$  between the true reaction plane and the planes A and B, respectively. For simplicity, we assume that the distributions  $P_A(\Phi)$  and  $P_B(\Phi)$  can be parameterized in terms of Eq. 2 with  $\omega = \text{constant}$ . The dashed curves in Fig. 21 show the convolutions of the individual reaction plane distributions, Eq. 25. From the convolution of the two-half sets, we extracted the shape of the distribution  $P_{\frac{1}{2}N}(\Delta\Phi)$ , shown by the dot-dashed curve. Using this information, we estimated the shape of the distribution,  $P_F(\Delta\Phi)$ , of fission plane orientations (dotted curve) from the relative distributions of the planes extracted for one half-subset and from fission. Finally, we made an estimate of the shape of the distribution,  $P_N(\Delta\Phi)$ , of planes extracted from all light particles and IMFs (solid curve). As might have been expected from Figs. 8 and 11, the estimated distributions  $P_F(\Delta\Phi)$  and  $P_N(\Delta\Phi)$  have similar azimuthal anisotropies for the present reaction, in qualitative agreement with the observations of ref. [49].

In order to obtain an estimate of the azimuthal distribution of the various trigger particles with respect to the true reaction plane, we assume that the accuracy of reaction plane determinations does not depend on the trigger particles. This assumption may not be strictly valid since different trigger particles may originate from collisions with different ranges of impact parameter characterized by different azimuthal distributions of the emitted particles. Furthermore, we assume that the experimental azimuthal distributions can be described by convolutions of the form of Eq. 25, where distributions A and B now represent the distributions of the trigger particle and of the experimentally determined reaction plane with respect to the true reaction plane, respectively. The distribution of fission planes,  $P_F(\Phi)$ , could have been taken from Fig. 21. Instead, the fission distribution, the individual trigger particle distributions and the distribution of planes,  $P_{N-1}(\Phi)$ , extracted from detected light particles and IMFs (excluding the trigger particle) were fitted simultaneously to the data shown in Fig. 8 and to angular correlations,  $P(\Delta\Phi_{F-(N-1)})$ , between the fission plane and the plane defined by the  $N-1$  light particles and IMFs which were detected in coincidence with the trigger particle. The fission distribution,  $P_F(\Phi)$ , extracted from this global fit displayed an azimuthal anisotropy coefficient of  $A_{\Phi, F} = 7.0 \pm 0.3$  consistent with the results shown in Fig. 21 and providing an additional cross

check for the accuracy of our previous results obtained by subdividing each event into two subsets containing equal numbers of particles. The extracted distribution  $P_{N-1}(\bar{\alpha})$  was found to be slightly less anisotropic than the distribution  $P_N(\bar{\alpha})$  shown by the solid curve in Fig. 21. This slight difference is consistent with the fact that, in Fig. 22, one less particle is used for the construction of transverse momentum tensor. Within the experimental uncertainties, the difference between the extracted distributions  $P_N(\bar{\alpha})$  and  $P_{N-1}(\bar{\alpha})$  is consistent with the calculated multiplicity dependence shown in Fig. 16.

For illustration, Fig. 22 gives a comparison of these global fits (solid curves) with the experimental distributions extracted by means of the transverse momentum tensor method (solid points). (Fits of similar quality are obtained for azimuthal distributions measured with respect to the fission plane.) For ease of presentation, all calculated distributions shown in the figure were normalized to  $P(0)=1$ , and the normalization of the experimental distributions was treated as a fit parameter. The dashed curves show the extracted distributions of the indicated trigger particles with respect to the true reaction plane. Quite clearly, all measured azimuthal distributions are strongly damped by the finite resolution with which the reaction plane is determined experimentally. For particles heavier than  $\alpha$ -particles, the measured azimuthal distributions are more sensitive to the limited accuracy of the experimental reaction plane determination and less sensitive to the azimuthal anisotropy of the underlying triple differential cross section of the trigger particle.

### VII. Summary and Conclusion

In this paper, we have investigated and compared various methods to determine the orientation of the entrance channel reaction plane from the distribution of detected particles. In order to allow a comparison of methods utilizing light particles and with that using fission fragments, we studied the asymmetric reaction  $^{36}\text{Ar} + ^{197}\text{Au}$  at  $E/A=35$  MeV.

For this reaction, very similar azimuthal correlations were observed with respect to the fission-plane and with respect to the plane defined by the orientation of the major axis of the transverse momentum tensor. The

reconstruction of the reaction plane was shown to improve with lower detector thresholds and when unidentified low-energy heavy fragments, stopped in the scintillator foils of our detectors, were incorporated into the analysis. Further improvements could be expected with detectors capable of identifying such particles and measuring their energies.

The convergence of the transverse momentum tensor method was explored via Monte Carlo simulations. The quality of reaction plane reconstruction was found to be sensitive to the azimuthal anisotropy of the average single particle distributions; it was only moderately sensitive to the multiplicity of detected particles. Exact knowledge of the weight functions, characterizing the dependence of azimuthal anisotropies on energy, angle, and particle type, was found to be of minor importance as long as known dependences were taken into account in an approximate way.

In situations in which the transverse momentum tensor method is close to optimal, one can obtain reasonably accurate information about the resolution of reaction plane reconstructions by dividing events into two parts, each with half of the original multiplicity, and determining the probability distribution of the angle between the reaction planes determined for each of these subsets. From this experimental probability distribution, one can unfold the resolution of reaction plane reconstructions for each of these parts in a fairly model independent fashion. Furthermore, the extrapolation of the resolution for the full event was found to be relatively insensitive to the functional form of the weight function. In practically all cases, the azimuthal distributions of trigger particles measured with respect to experimentally determined reaction planes were found to be strongly damped by the accuracy with which the reaction plane can be determined experimentally.

Detailed comparisons of experimentally measured triple differential cross sections with theoretical predictions must account for the intrinsic resolutions with which the reaction plane was reconstructed. The accuracy of reaction plane reconstructions was shown to depend strongly on the azimuthal anisotropies of the detected particles which are largest for complex particles. On the other hand, many microscopic theories presently predict only

single-nucleon distributions. In order to be able to make quantitative comparisons of experimental triple differential cross sections with predictions of single-particle theories one must solve the problem of relating the azimuthal distributions of nucleons to those of complex particles.

Helpful discussions with G. Bertsch, P. Danielewicz, and K. Wilson are gratefully acknowledged. This work is based upon work supported by the National Science Foundation under Grant numbers PHY-86-11210, PHY-89-13815. WGL acknowledges the receipt a of U.S. Presidential Young Investigator Award and NC acknowledges partial support by the FAPESP, Brazil.

## References

- † Present address: Instituto de Física, Universidade de São Paulo, C. Postal 20516, CEP 01498, São Paulo, Brazil
1. G.F. Bertsch, H. Kruse, and S. Das Gupta, Phys. Rev. C29, 673 (1984).
  2. H. Kruse, B.V. Jacak, and H. Stöcker, Phys. Rev. Lett. 54, 289 (1985).
  3. H. Kruse, B.V. Jacak, J.J. Molitoris, G.D. Westfall, and H. Stöcker, Phys. Rev. C31, 1170 (1985).
  4. J. Aichelin and G. Bertsch, Phys. Rev. C31, 1730 (1985).
  5. G.F. Bertsch and S. Das Gupta, Phys. Rep. 160, 189 (1988).
  6. J.J. Molitoris and H. Stöcker, Phys. Lett. B162, 47 (1985).
  7. J.J. Molitoris and H. Stöcker, Phys. Rev. C32, 346 (1985).
  8. J. Aichelin and H. Stöcker, Phys. Lett. B176, 14 (1986).
  9. C. Grégoire, B. Remaud, F. Sébille, L. Vinet, and Y. Raffray, Nucl. Phys. A465, 317 (1986).
  10. J. Aichelin, A. Rosenhauer, G. Peilert, H. Stöcker, and W. Greiner, Phys. Rev. Lett. 58, 1926 (1987).
  11. C. Gale, G. Bertsch, and S. Das Gupta, Phys. Rev. C35, 1666 (1987).
  12. W. Bauer, G.F. Bertsch, and S. Das Gupta, Phys. Rev. Lett. 58, 863 (1987).
  13. G.F. Bertsch, W.G. Lynch, and M.B. Tsang, Phys. Lett. B189, 384 (1987).
  14. G.M. Welke, M. Prakash, T.T.S. Kuo, S. Das Gupta, and C. Gale, Phys. Rev. C38, 2101 (1988).
  15. D.H. Boal and J.N. Gosli, Phys. Rev. C37, 91 (1988).
  16. J. Aichelin, G. Peilert, A. Bohnet, A. Rosenhauer, H. Stöcker, and W. Greiner, Phys. Rev. C37, 2451 (1988).
  17. G. Peilert, H. Stöcker, W. Greiner, A. Rosenhauer, A. Bohnet, and J. Aichelin, Phys. Rev. C39, 1402 (1989).
  18. M.B. Tsang, G.F. Bertsch, W.G. Lynch, and M. Tohyama, Phys. Rev. C40, 1685 (1989).
  19. D.H. Boal and J.N. Gosli, Phys. Rev. C42, R502 (1990).
  20. D.H. Boal and J.C.K. Wong, Phys. Rev. C41, 118 (1990).
  21. H.M. Xu, W.G. Lynch, P. Danielewicz, and G.F. Bertsch, Phys. Rev. Lett. 65, 843 (1990).
  22. P. Danielewicz and G. Odyniec, Phys. Lett. B157, 146 (1985).

23. P. Danielewicz, H. Ströbele, G. Odyniec, D. Bangert, R. Bock, R. Brockmann, J.W. Harris, H.G. Pugh, W. Rauch, R.E. Renfordt, A. Sandoval, D. Schall, L.S. Schroeder, and R. Stock, Phys. Rev. C38, 120 (1988).
24. K.G.R. Doss, H.Å. Gustafsson, H.H. Gutbrod, K.H. Kampert, B. Kolb, H. Löhner, B. Ludewigt, A.M. Poskanzer, H.G. Ritter, H.R. Schmidt, and H. Wieman, Phys. Rev. Lett. 57, 302 (1986).
25. K.G.R. Doss, H.Å. Gustafsson, H.H. Gutbrod, J.W. Harris, B.V. Jacak, K.H. Kampert, B. Kolb, A.M. Poskanzer, H.G. Ritter, H.R. Schmidt, L. Teitelbaum, M. Tincknell, S. Weiss, and H. Wieman, Phys. Rev. Lett. 59, 2720 (1987).
26. H.H. Gutbrod, K.H. Kampert, B.W. Kolb, A.M. Poskanzer, H.G. Ritter, and H.R. Schmitt, Phys. Lett. B216, 267 (1989).
27. H.H. Gutbrod, K.H. Kampert, B.W. Kolb, A.M. Poskanzer, H.G. Ritter, R. Schicker, and H.R. Schmitt, Phys. Rev. C42, 640 (1990).
28. D. Krofcheck, W. Bauer, G.M. Crawley, C. Djalali, S. Howden, C.A. Ogilvie, A. VanderMolen, G.D. Westfall, W.K. Wilson, R.S. Tickle, and C. Gale, Phys. Rev. Lett. 63, 2028 (1988).
29. D. Krofcheck, D. Cebra, M. Cronqvist, R. Lacey, T. Li, C.A. Ogilvie, A. VanderMolen, K. Tyson, G.D. Westfall, W.K. Wilson, J.S. Winfield, A. Nadasen, and E. Norbeck, Phys. Rev. C43, 350 (1991).
30. C.A. Ogilvie, D.A. Cebra, J. Clayton, P. Danielewicz, S. Howden, J. Karn, A. Nadasen, A. Vander Molen, G.D. Westfall, W.K. Wilson, and J.S. Winfield, Phys. Rev. C40, 2592 (1989).
31. C.A. Ogilvie, W. Bauer, D.A. Cebra, J. Clayton, S. Howden, J. Karn, A. Nadasen, A. Vander Molen, G.D. Westfall, W.K. Wilson, and J.S. Winfield, Phys. Rev. C42, R10 (1990).
32. J.P. Sullivan, J. Péter, D. Cussol, G. Bizard, P. Brou, M. Louvel, J.P. Patry, E. Regimbart, J.C. Steckmeyer, B. Tamain, E. Crema, H. Doubre, K. Hagel, G.M. Jin, A. Péghaire, F. Saint-Laurent, Y. Cassagnou, R. Legrain, C. Lebrun, E. Rosato, R. McGrath, S.C. Jeong, S.M. Lee, Y. Nagashima, T. Nakagawa, M. Ogihara, J. Kasagi, and T. Motobayashi, Phys. Lett. B249, 8 (1990).
33. R. Stock, Phys. Reports. 135, (1986) 259.
34. H. Stöcker and W. Greiner, Phys. Reports 137, 277 (1986).

35. C. Cavata, M. Demoullins, J. Gosset, M.C. Lemaire, D. L'Hôte, J. Poitou, and O. Valette, Phys. Rev. C42, 1760 (1990).
36. T.C. Awes, G. Poggi, C.K. Gelbke, B.B. Back, B.G. Glagola, and V.E. Viola, Jr., Phys. Rev. C24, 89, (1981).
37. Z. Chen, C.K. Gelbke, J. Pochodzalla, C.B. Chitwood, D.J. Fields, W.G. Gong, W.G. Lynch, and M.B. Tsang, Nucl. Phys. A473, 564 (1987).
38. M.B. Tsang, Y.D. Kim, N. Carlin, Z. Chen, R. Fox, C.K. Gelbke, W.G. Gong, W.G. Lynch, T. Murakami, T.K. Nayak, R.M. Ronningen, H.M. Xu, F. Zhu, L. Sobotka, D. Stracener, D.G. Sarantites, Z. Majka, V. Abenante, and H. Griffin, Phys. Lett. B220, 492 (1989).
39. C.A. Ogilvie, D. Cebra, J. Clayton, S. Howden, J. Karn, A. VanderMolen, G.D. Westfall, W.K. Wilson, and J.S. Winfield, Phys. Rev. C40, 654 (1989).
40. J. Galin, Nucl. Phys. A447 (1985) 519c.
41. M. Morjean, et al., Phys. Lett. B203 (1988) 215.
42. W.K. Wilson, W. Benenson, D.A. Cebra, J. Clayton, S. Howden, J. Karn, T. Li, C.A. Ogilvie, A. VanderMolen, G.D. Westfall, J.S. Winfield, and A. Nadasen, Phys. Rev. C41, R1881 (1990).
43. W.K. Wilson, Ph.D. Dissertation, Michigan State University, 1991, unpublished and private communication.
44. M.B. Tsang, C.B. Chitwood, D.J. Fields, C.K. Gelbke, D.R. Klesch, W.G. Lynch, K. Kwiatkowski and V.E. Viola, Jr., Phys. Rev. Lett. 52, 1967 (1984).
45. M.B. Tsang, W.G. Lynch, C.B. Chitwood, D.J. Fields, D.R. Klesch, C.K. Gelbke, G.R. Young, T.C. Awes, R.L. Ferguson, F.E. Obenshain, F. Plas11 and R.L. Robinson, Phys. Lett. 148B, 265 (1984).
46. C.B. Chitwood, D.J. Fields, C.K. Gelbke, D.R. Klesch, W.G. Lynch, M.B. Tsang, T.C. Awes, R.L. Ferguson, F.E. Obenshain, F. Plas11, R.L. Robinson, and G.R. Young, Phys. Rev. C34, 858 (1986).
47. M.B. Tsang, R.M. Ronningen, G. Bertsch, Z. Chen, C.B. Chitwood, D.J. Fields, C.K. Gelbke, W.G. Lynch, T. Nayak, J. Pochodzalla, T. Shea, and W. Trautmann, Phys. Rev. Lett. 57, 559 (1986).
48. M.B. Tsang, W.G. Lynch, R.M. Ronningen, Z. Chen, C.K. Gelbke, T. Nayak, J. Pochodzalla, F. Zhu, M. Tohyama, W. Trautmann, and W. Dünneweber, Phys. Rev. Lett. 60, 1479 (1988).



49. M.B. Tsang, Y.D. Kim, N. Carlin, Z. Chen, C.K. Gelbke, W.G. Gong, W.G. Lynch, T. Murakami, T. Nayak, R.M. Ronningen, H.M. Xu, F. Zhu, L.G. Sobotka, D.W. Stracener, D.G. Sarantites, Z. Majka, and V. Abenante, Phys. Rev. C42, R15 (1990).
50. D.J. Fields, W.G. Lynch, T.K. Nayak, M.B. Tsang, C.B. Chitwood, C.K. Gelbke, R. Morse, J. Wilczynski, T.C. Awes, R.L. Ferguson, F. Plasil, F.E. Obenshain, and G.R. Young, Phys. Rev. C34, 536 (1986).
51. R.T. de Souza, N. Carlin, Y.D. Kim, J. Ottarson, L. Phair, D.R. Bowman, C.K. Gelbke, W.G. Gong, W.G. Lynch, R.A. Pelak, T. Peterson, G. Poggi, M.B. Tsang, and H.M. Xu, Nucl. Instr. and Meth. A295, 109 (1990).
52. M.B. Tsang, D.R. Bowman, N. Carlin, P. Danielewicz, R.T. de Souza, C.K. Gelbke, W.G. Gong, Y.D. Kim, W.G. Lynch, L. Phair, and F. Zhu, to be published.
53. W.G. Lynch, L.W. Richardson, M.B. Tsang, R.E. Ellis, C.K. Gelbke and R.E. Warner, Phys. Lett. B108, 274 (1982).
54. J. Knoll, Nucl. Phys. A343, 511 (1980).
55. W.G. Meyer, H.H. Gutbrod, C. Lukner, and A. Sandoval, Phys. Rev. C22, 179 (1980).
56. S.B. Kaufman, M.S. Freedman, D.J. Henderson, E.P. Steinberg, B.D. Wilkins, A. Baden, H.H. Gutbrod, M.R. Meier, J. Péter, H.G. Ritter, H. Stelzer, A.I. Warwick, H.H. Wieman, and F. Weik, Phys. Rev. C26, 2694 (1982).
57. A.I. Warwick, H.H. Wieman, H.H. Gutbrod, M.R. Maier, J. Péter, H.G. Ritter, H. Stelzer, F. Weik, M. Freedman, D.J. Henderson, S.B. Kaufman, E.P. Steinberg, and B.D. Wilkins, Phys. Rev. C27, 1083 (1983).

*Tables*

**Table 1:** Coverage in solid angle, polar and azimuthal angles for individual detectors of the Miniball. Ring 1 was not used in this experiment.

Ring #	$\theta$ (deg)	$\Delta\Omega$ (msr)	$\Delta\theta$ (deg)	$\Delta\phi$ (deg)
1	12.5	13.1	7	30
2	19.5	15.4	7	22.5
3	27.0	18.5	8	18.0
4	35.5	22.5	9	15.0
5	45.0	30.2	10	15.0
6	57.5	65.9	15	18.0
7	72.5	72.7	15	18.0
8	90.0	93.3	20	20.0
9	110.0	134.2	20	25.7
10	130.0	132.0	20	30.0
11	150.0	136.2	20	45.0

**Table 2:** Parameters used in the Monte-Carlo simulations of the reaction plane reconstruction.  $E_l$  and  $E_h$  denote the low and high energy limits of the transverse energy spectra used in the calculations.

mass number	weight	T (MeV)	$E_l$ (MeV)	$E_h$ (MeV)
1	2.22	7.48	3	150
2	0.86	9.69	5	150
3	0.55	10.63	8	150
4	2.00	9.64	10	200

### Figure Captions

Fig. 1: Azimuthal correlations between low-energy heavy fragments detected in rings 3-7,9,and 10. The solid curve shows the inclusive correlations; the other curves show correlations when a trigger particle with the indicated transverse momentum is emitted at  $\theta=45^\circ$  and normal to the fission plane.

Fig. 2: Family of azimuthal distributions with respect to the reaction plane described by Eq. 2. The curves are labelled by the azimuthal anisotropy coefficient, Eq. 10.

Fig. 3: Relation between weight function, variance and azimuthal anisotropy coefficient for the family of curves described by Eq. 2. (For definitions, see Eqs. 9, 10.)

Fig. 4: Energy spectra of particles detected in Ring 5 (centered at  $\theta_{lab}=45^\circ$ ). The sharp cut-offs in the energy spectra of the hydrogen isotopes at  $E_p \approx 70$  MeV,  $E_d = 100$  MeV, and  $E_t = 120$  MeV reflect software gates eliminating particles punching through the CsI(Tl) crystals.

Fig. 5: Transverse energy spectra measured in this experiment. The solid curves show the exponential approximation to these energy spectra used in the Monte Carlo calculations shown in Figs. 18-21. The sharp drop in the energy spectra at high energies is an experimental artifact due to particles punching through the detectors.

Fig. 6: Two-dimensional contour diagram of the relative probabilities for detecting a total of  $N_C$  identified charged particles of which  $N_{IMF}$  particles are identified intermediate mass fragments ( $Z \geq 3$ ).

Fig. 7: Charged particle (left hand panel) and (IMF) multiplicity distributions measured inclusively (solid points) and in coincidence with fission fragments (open points).

**Fig. 8:** Azimuthal distributions of particles measured with respect to the fission plane, Eq. 1 (open points), and with respect to the plane determined from the major axis of the transverse momentum tensor, Eq. 12 (solid points). The elemental charge of the trigger particles, emitted at  $\theta=45^\circ$ , is indicated in the individual panels; the energy gates for the trigger particles were  $E/A=12-20$  MeV.

**Fig. 9:** Dependence of the azimuthal anisotropy coefficient for Li fragments upon the assumed mass  $A$  of a recoiling source when one corrects for recoil effects by means of Eq. 21 and determines the orientation of the reaction plane from Eq. 12. An energy gate of  $E/A > 8$  MeV was applied to the Li trigger fragments.

**Fig.10:** Distributions,  $P(\Delta\Phi)$ , of relative azimuthal orientations between planes determined by various methods.  $\Phi_F$  is the azimuthal orientation of the fission plane, Eq. 1;  $\Phi_{PT}$  and  $\Phi_{rot}$  denote azimuthal orientations of the planes extracted from the light particle and intermediate mass fragment distributions by means of Eqs. 12 and 18, respectively. Solid and open points:  $|\Phi_F - \Phi_{PT}|$  distributions for all events and for events with at least one energetic ( $E_\alpha > 80$  MeV)  $\alpha$ -particle detected in rings 4-7.

**Fig.11:** Azimuthal anisotropy coefficients with respect to planes determined from fission, Eq. 1 (open points), from the light-particle and IMF emission patterns, Eq. 12 (solid points), and with the inclusion of unidentified low-energy heavy fragments, Eqs. 12 and 22 (open squares). Different panels show results for different energies of the trigger particles.

**Fig.12:** Variances of azimuthal distributions with respect to planes determined from fission, Eq. 1 (open points), from the light-particle and IMF emission patterns, Eq. 12 (solid points), and with the inclusion of unidentified low-energy heavy fragments, Eqs. 12 and 22 (open squares). Different panels show results for different energies of the trigger particles.

**Fig.13:** Azimuthal anisotropy coefficients with respect to planes determined from the light-particle and IMF emission patterns, Eq. 12 (solid points); and

with the inclusion of unidentified low-energy heavy fragments, Eqs. 12 and 22 (open squares). Different panels show results for different energies of the trigger particles. Events were presorted by the requirement of  $N=4-9$  and at least one low-energy heavy fragment in the exit channel.

Fig.14: Influence of particle detection thresholds on azimuthal anisotropy coefficients determined by means of Eq. 12. The applied energy thresholds are indicated in the figure. Minimum energy thresholds of the detector are given in Section II.

Fig.15: Probability distributions  $P(\Delta\Phi)$  for the angular difference  $\Delta\Phi$  between the true and reconstructed reaction planes. The azimuthal distributions of the emitted particles were assumed to have the form of Eq. 2 with constant weight functions,  $\omega=\text{constant}$ . Different panels show results for different azimuthal anisotropy coefficients, Eq. 10, characterizing the single particle distributions. The curves are labelled by the number of particles used for the reconstruction of the reaction plane.

Fig.16: Variances for probability distributions  $P(\Delta\Phi)$  for the angle,  $\Delta\Phi$ , between the true and reconstructed reaction plane (Eq. 5) as a function of particle multiplicity  $N$ . The different curves are labelled by the azimuthal anisotropy coefficients characterizing the single particle distributions. Solid and dashed curves show the results for weight functions  $\omega=\text{constant}$  and  $\omega=\epsilon\sin\theta$ , respectively.

Fig.17: Probability distributions  $P(\Delta\Phi)$  for the angular difference  $\Delta\Phi$  between the true and reconstructed reaction planes. The azimuthal distributions of the emitted particles were assumed to have the form of Eq. 2 with  $\omega=\text{constant}$  (left hand panels) and  $\omega=\epsilon\sin\theta$  (right hand panels). The solid curves show the results obtained by using the optimum relation, Eq. 5, and the dashed curves show the results obtained by applying Eq. 12. Averages over light particles ( $A=1-4$ ) were performed with realistic weights. The top and bottom panels show results for two different azimuthal anisotropy coefficients ( $A_\phi=1.4$  and  $2.0$ ) for the average single particle distribution. The curves are labelled by the number of particles used for the reconstruction of the reaction plane.

**Fig.18:** The points show distributions  $P(\Delta\bar{\Phi}_{12})$  for the angle  $\Delta\bar{\Phi}_{12}$  between two reaction planes, each extracted from subsets of detected particles containing half the total event multiplicity using the transverse momentum tensor method, Eq. 12. The left hand panel shows the distribution extracted from identified light particles and intermediate mass fragments; the right hand panel shows the distribution obtained by also including unidentified low-energy heavy fragments according to Eq. 22. The solid lines show results of Monte-Carlo calculations for the distribution  $P(\Delta\bar{\Phi}_{12})$  using  $N=8$  and  $\omega=\epsilon\sin\theta$  with  $\epsilon$  adjusted to reproduce the data. The dot-dashed and dashed curves show the calculated distributions  $P_{\frac{1}{2}N}(\Delta\bar{\Phi})$  and  $P_N(\Delta\bar{\Phi})$  for the relative orientations between the true reaction plane and the planes reconstructed from  $\frac{1}{2}N=4$  and  $N=8$  particles, respectively.

**Fig.19:** The open points show the relation between azimuthal anisotropy parameters ( $A_{\bar{\Phi}_{12}}$  and  $A_{\bar{\Phi}_{\frac{1}{2}N}}$ ) and variances ( $\langle\Delta\bar{\Phi}_{12}^2\rangle^{1/2}$  and  $\langle\Delta\bar{\Phi}_{\frac{1}{2}N}^2\rangle^{1/2}$ ) of distributions  $P(\Delta\bar{\Phi}_{12})$  and  $P_{\frac{1}{2}N}(\Delta\bar{\Phi})$  obtained by the Monte Carlo simulations described in the text. The curves show the relation obtained with Eq. 23, when one approximates the distributions  $P_{\frac{1}{2}N}(\phi)$  by analytical functions,  $P_{\frac{1}{2}N}(\phi) \propto \exp(-\omega^2 \sin^2\phi)$ .

**Fig.20:** Relation between the variances,  $\langle\Delta\bar{\Phi}_{\frac{1}{2}N}^2\rangle^{1/2}$  and  $\langle\Delta\bar{\Phi}_N^2\rangle^{1/2}$ , of distributions,  $P_{\frac{1}{2}N}(\Delta\bar{\Phi})$  and  $P_N(\Delta\bar{\Phi})$ , calculated for a broad range of multiplicities and parameters  $\epsilon$  and  $\omega_0$ . Open and solid points represent calculations with momentum dependent ( $\omega=\epsilon\sin\theta$ ) and momentum independent ( $\omega=\omega_0$ ) weight functions, respectively. The curve represents a polynomial fit, Eq. 24.

**Fig.21:** Distributions for the relative orientations of planes determined from two half-subsets of light particles and IMFs (solid points), from one such half-subset and from fission (star shaped points), and from the full set of light particles and IMFs and from fission (open squares). The dashed curves represent convolutions of the estimated distributions,  $P_{\frac{1}{2}N}(\Delta\bar{\Phi})$ ,  $P_N(\Delta\bar{\Phi})$ , and  $P_F(\Delta\bar{\Phi})$ , shown by the dot-dashed, solid, and dotted curves, respectively.

Fig.22: Azimuthal distributions of the various trigger particles with respect to the measured reaction plane (solid points). Dashed curves show assumed distribution with respect to the true reaction plane. Solid curves show the results obtained by the convolution described in the text.

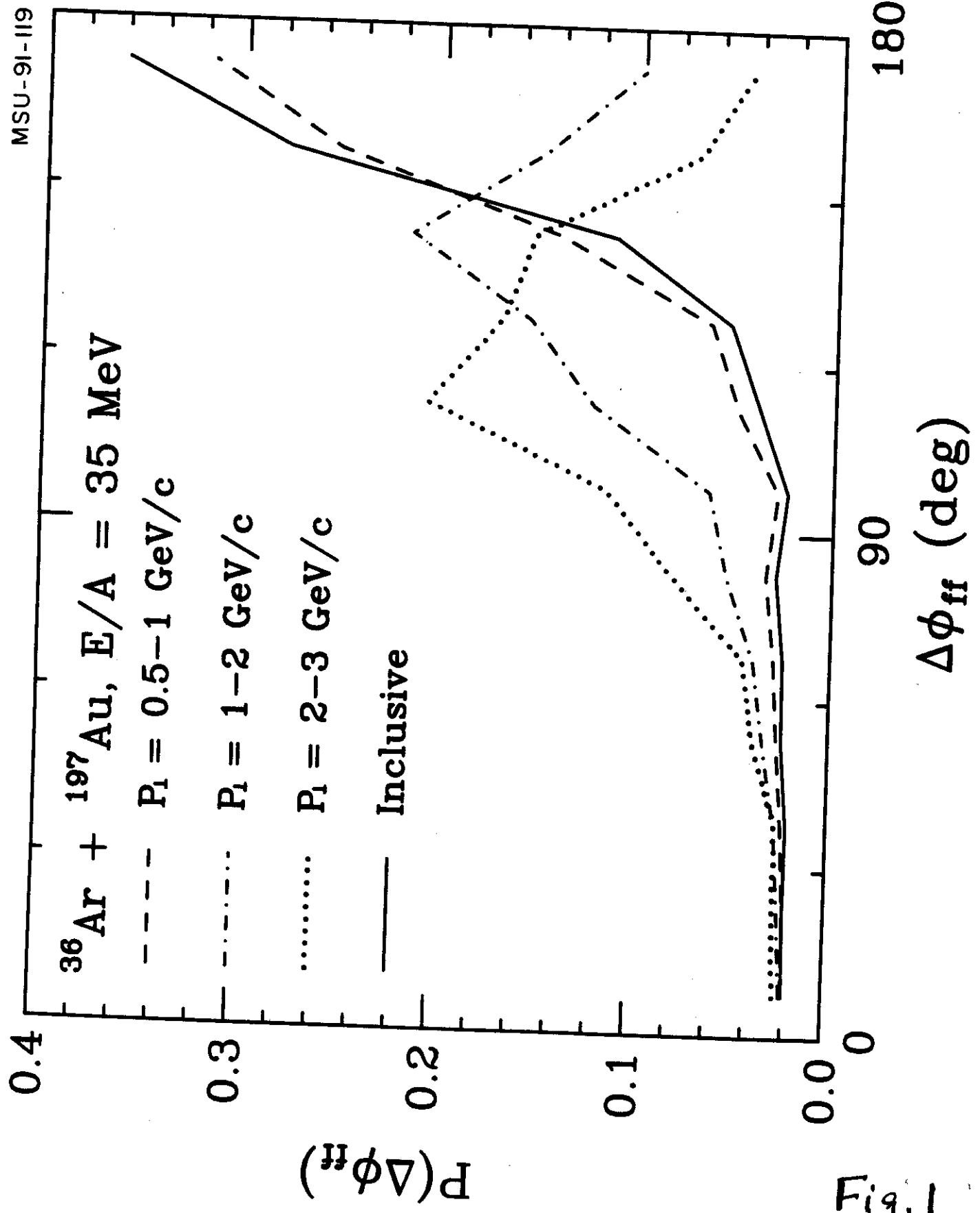


Fig. 1



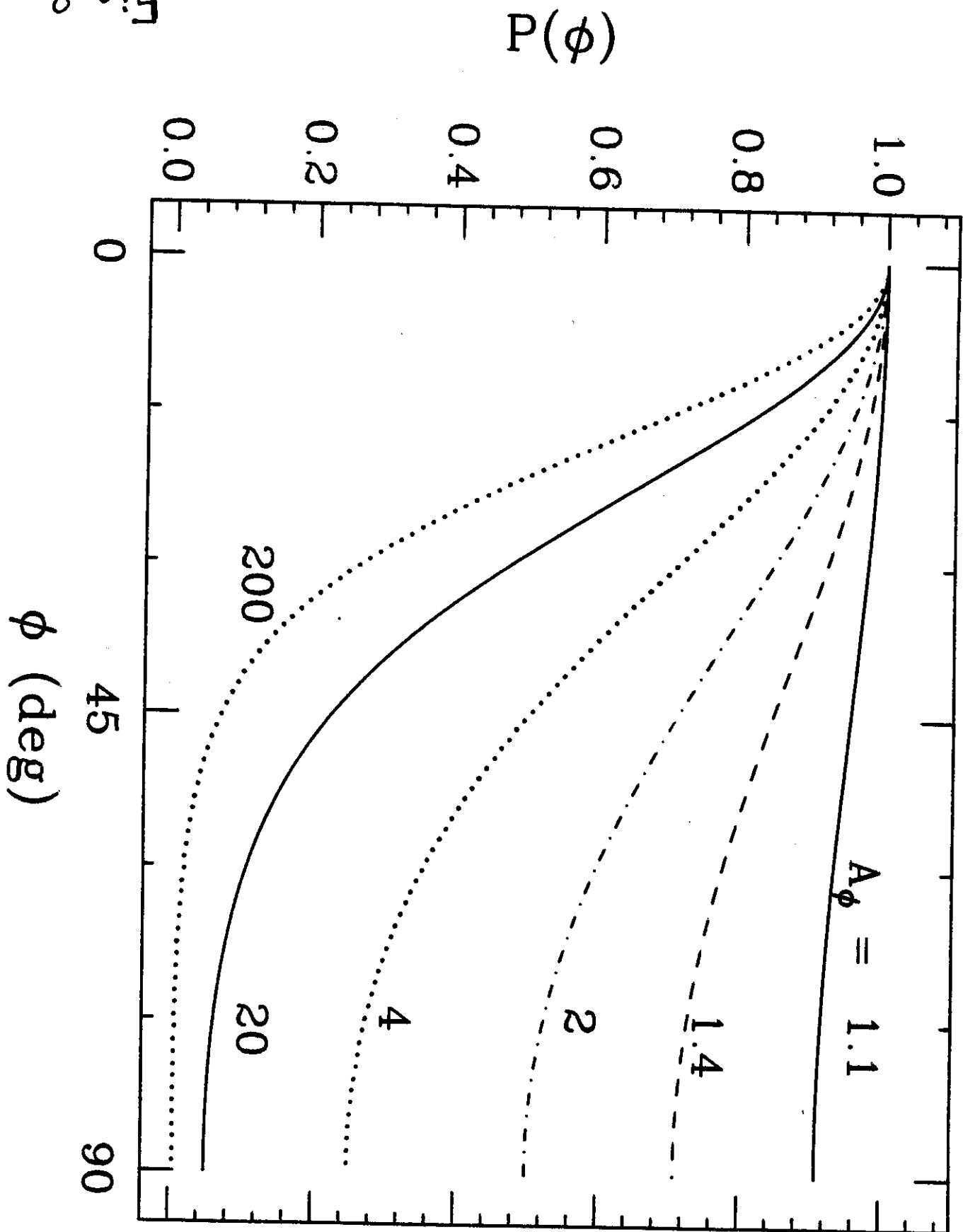


Fig. 2

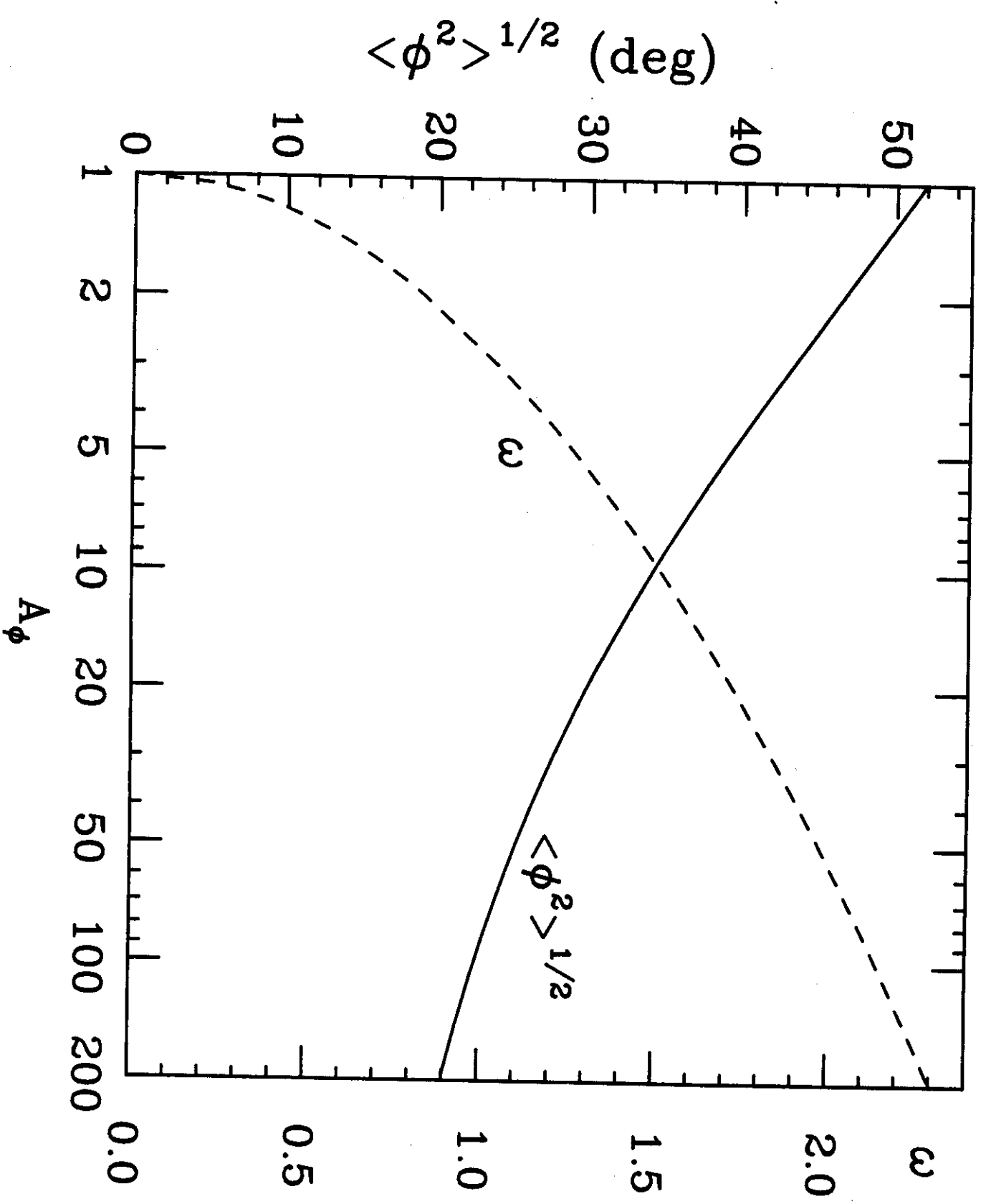


Fig. 5

$^{36}\text{Ar} + ^{197}\text{Au}$ ,  $E/A = 35\text{MeV}$ ,  $\theta_{\text{lab}} = 45^\circ$

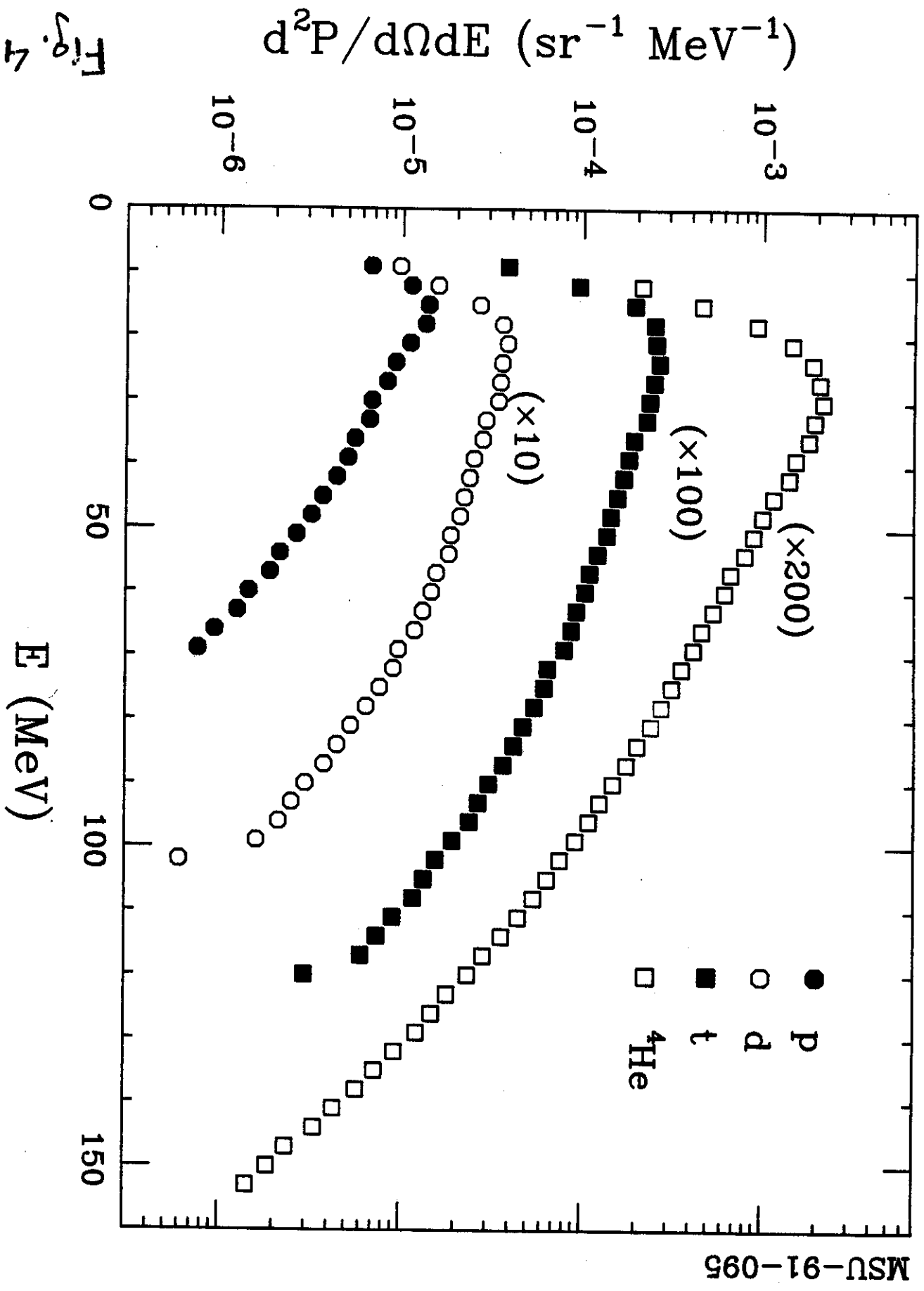
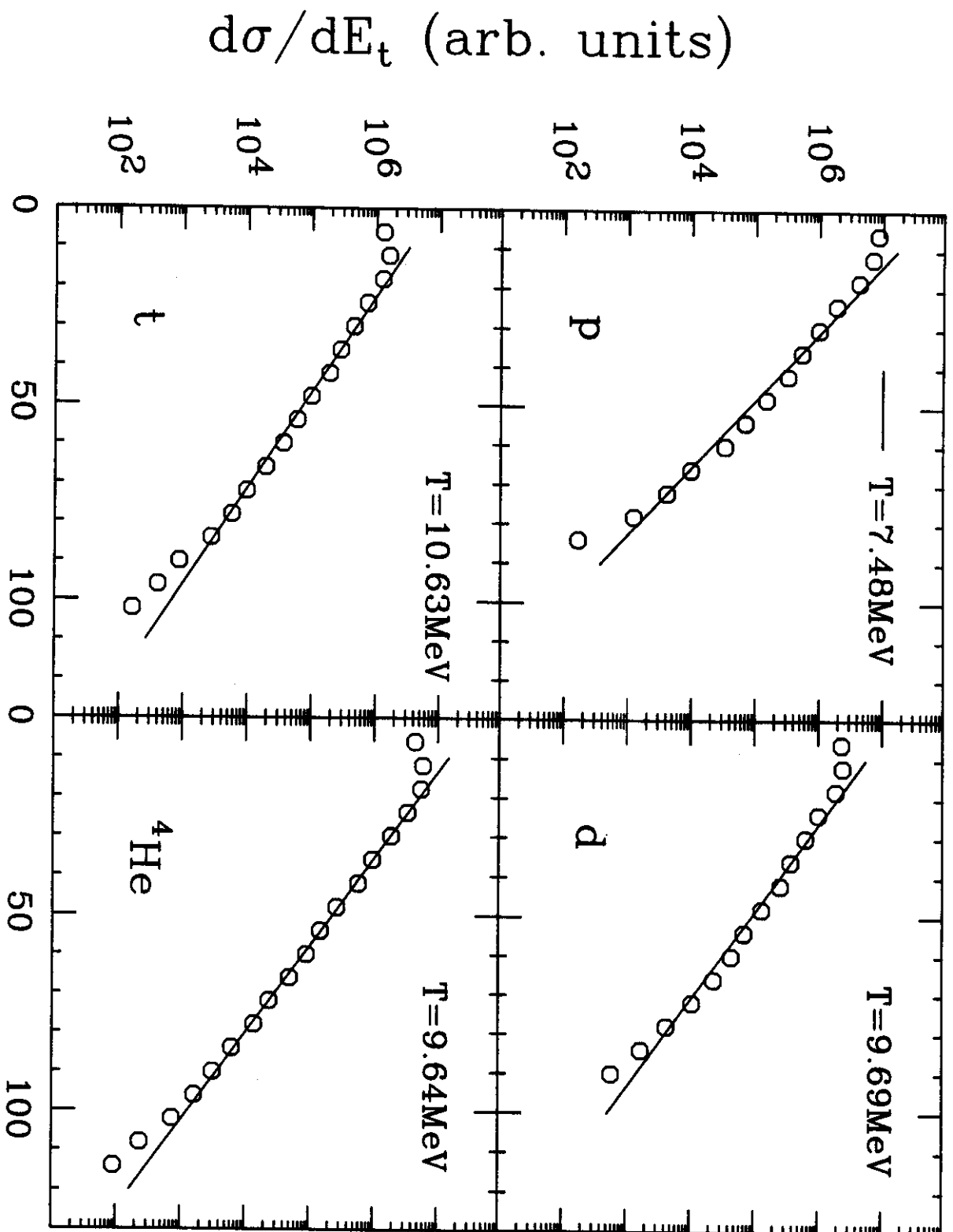


Fig. 4

$^{36}\text{Ar} + ^{197}\text{Au}$ ,  $E/A = 35\text{MeV}$



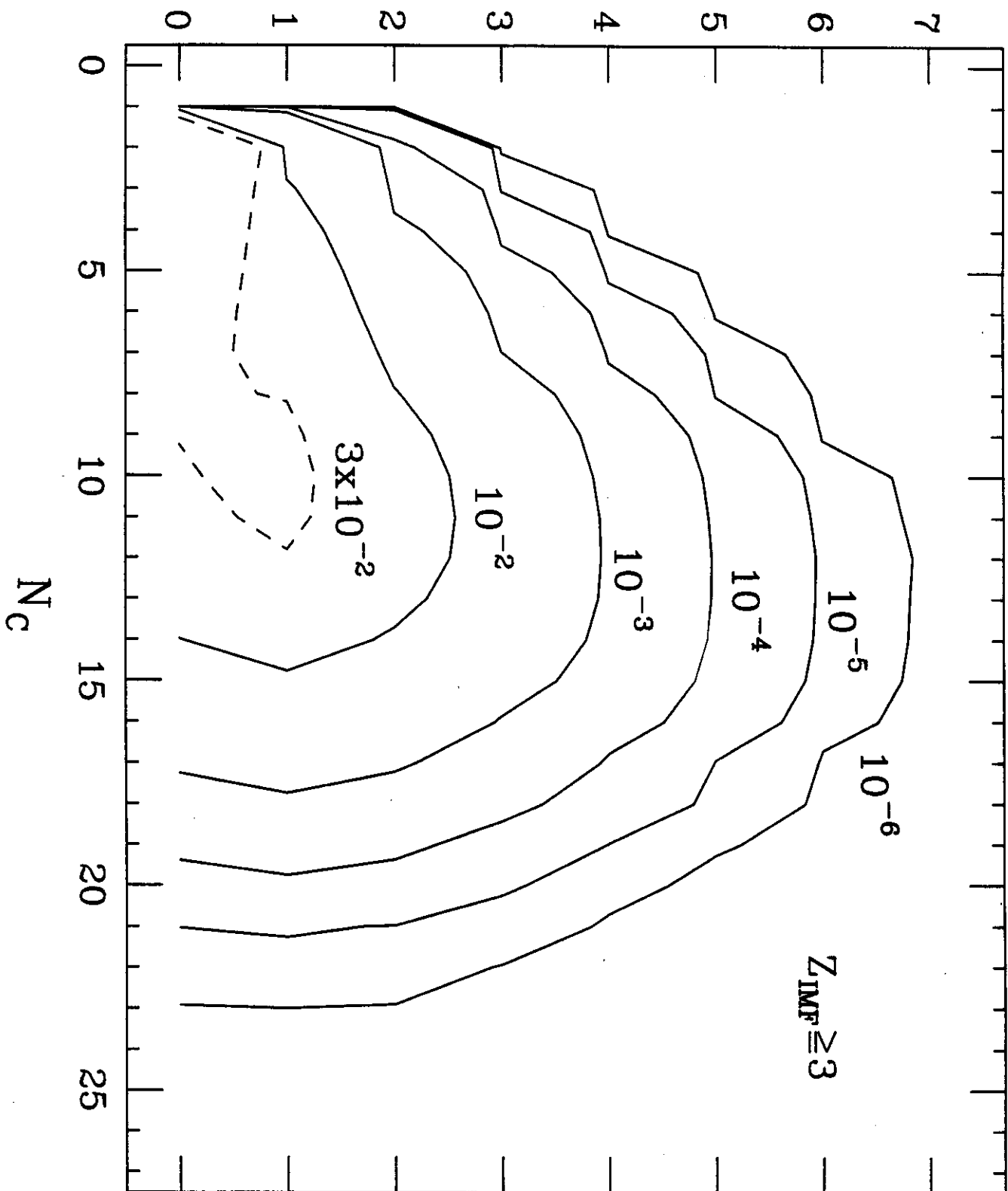
MSU-91-092

$d\sigma/dE_t$  (arb. units)

$E_t$  (MeV)

Fig. 5

$^{36}\text{Ar} + ^{197}\text{Au}$ ,  $E/A = 35\text{MeV}$



MSU-91-074

$N_{\text{IMF}}$

$N_C$

Fig. 6

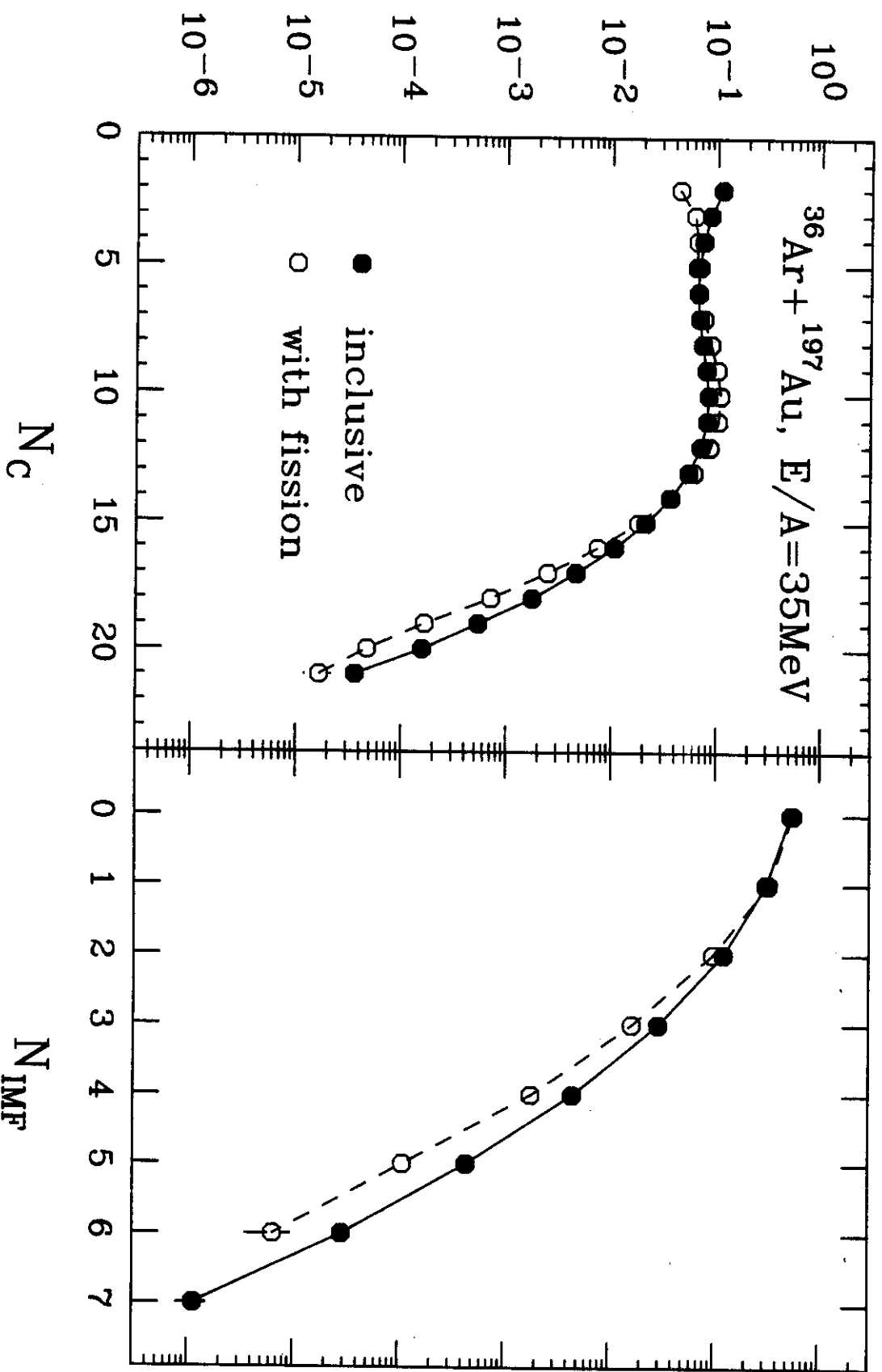
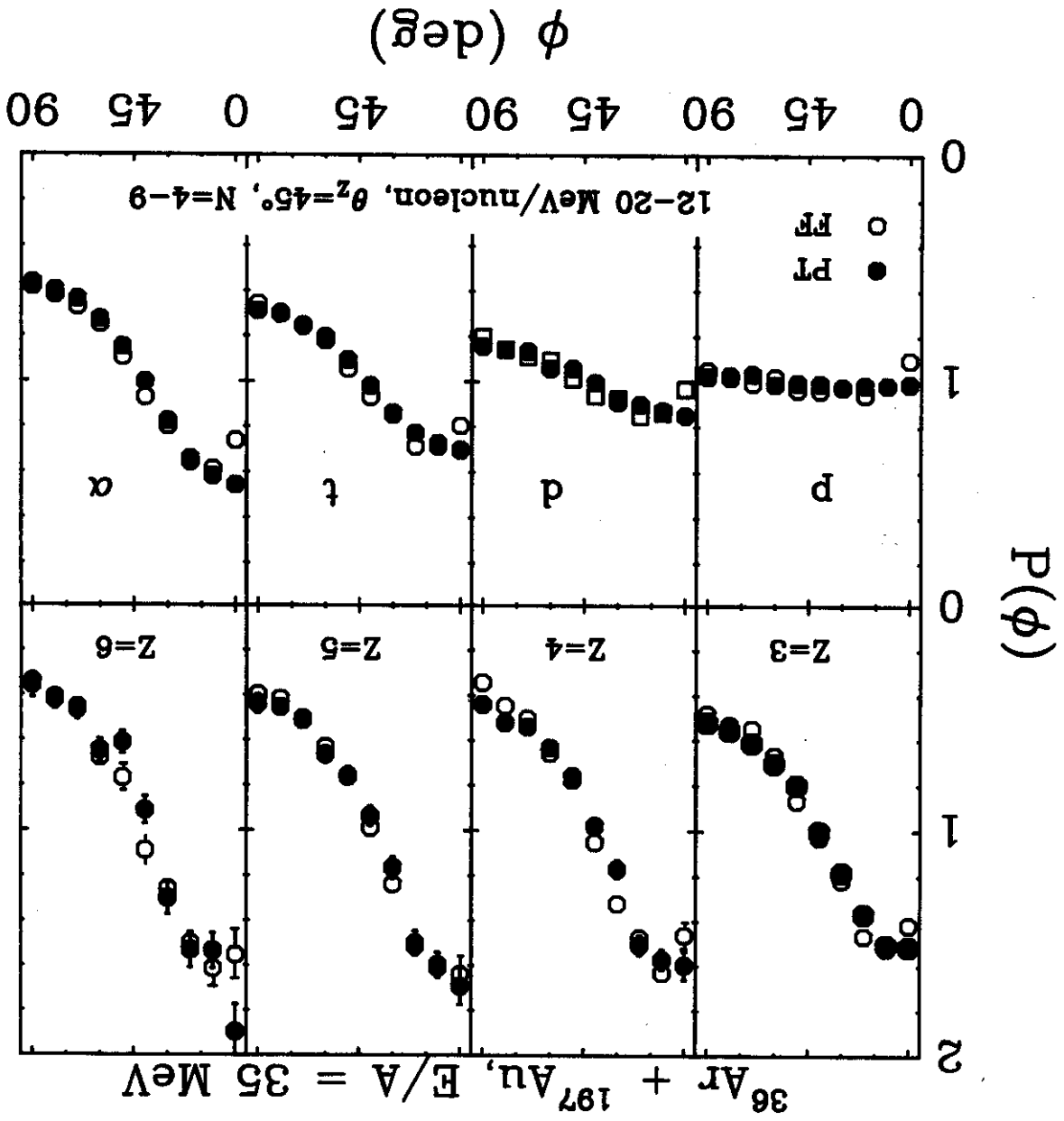


Fig. 7

Fig 8



$^{36}\text{Ar} + ^{197}\text{Au}$ ,  $E/A = 35 \text{ MeV}$

$Z=3$

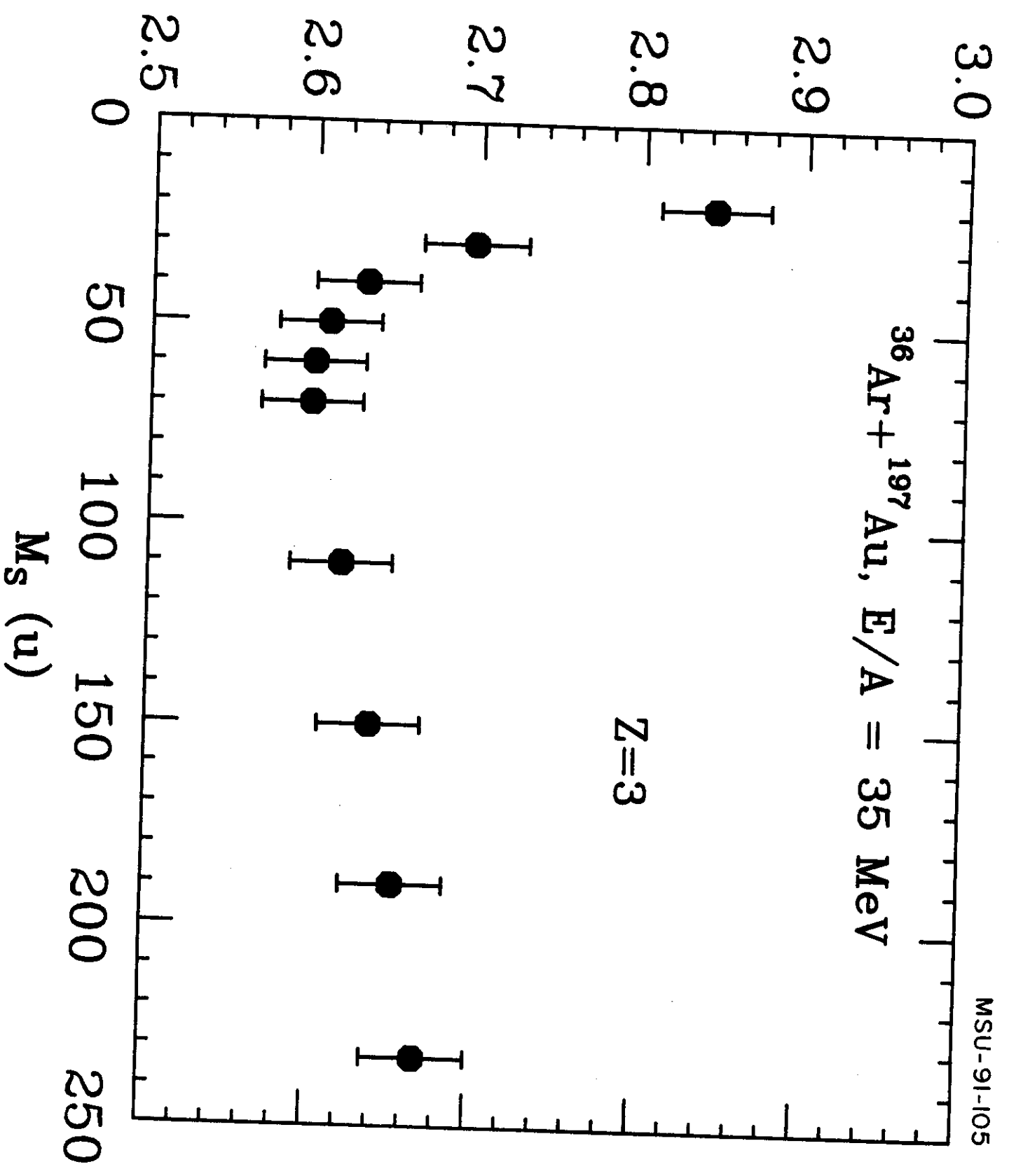
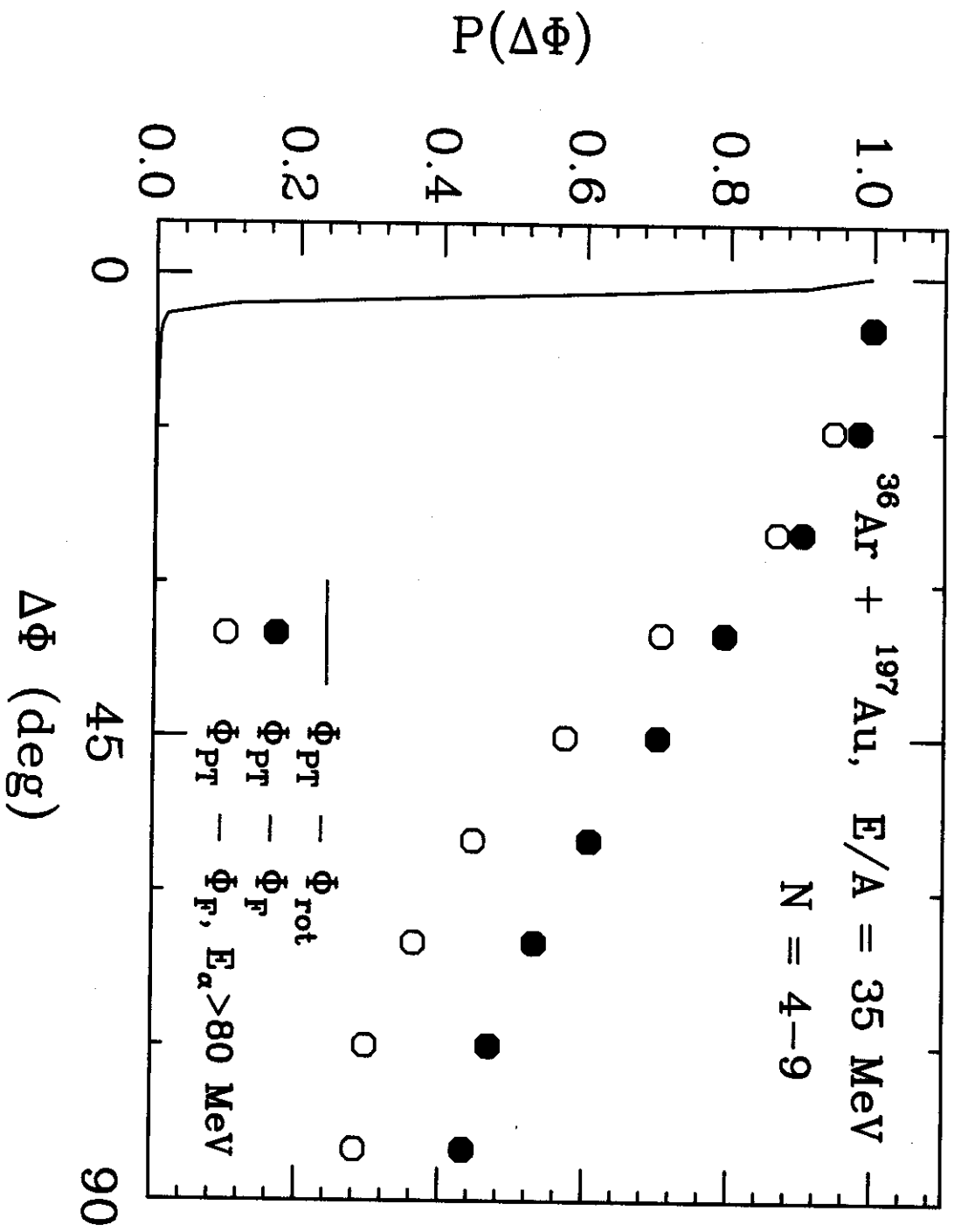


Fig. 9



Fig 10



MSU-91-133

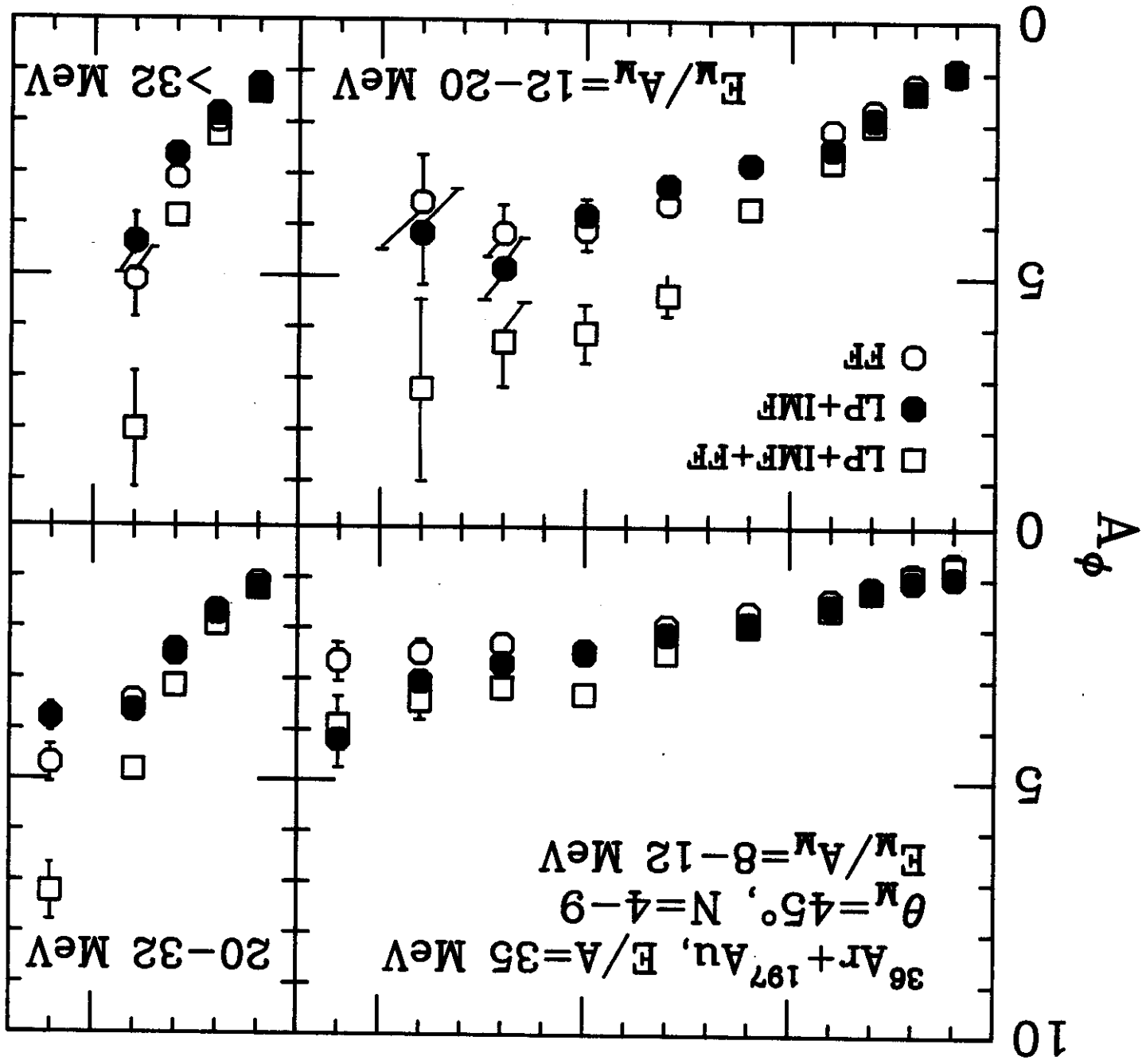


Fig. 11

Fig. 12

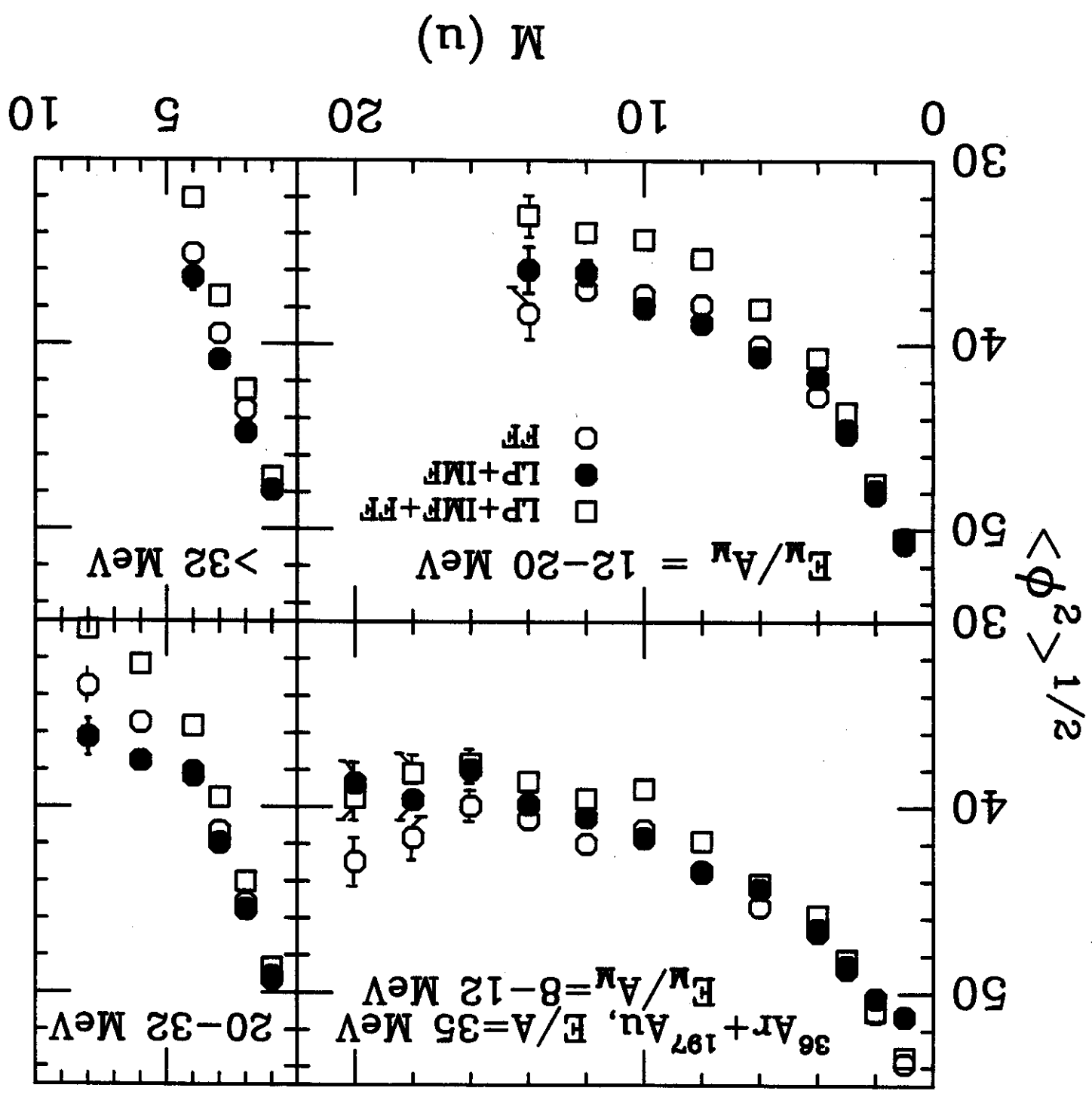
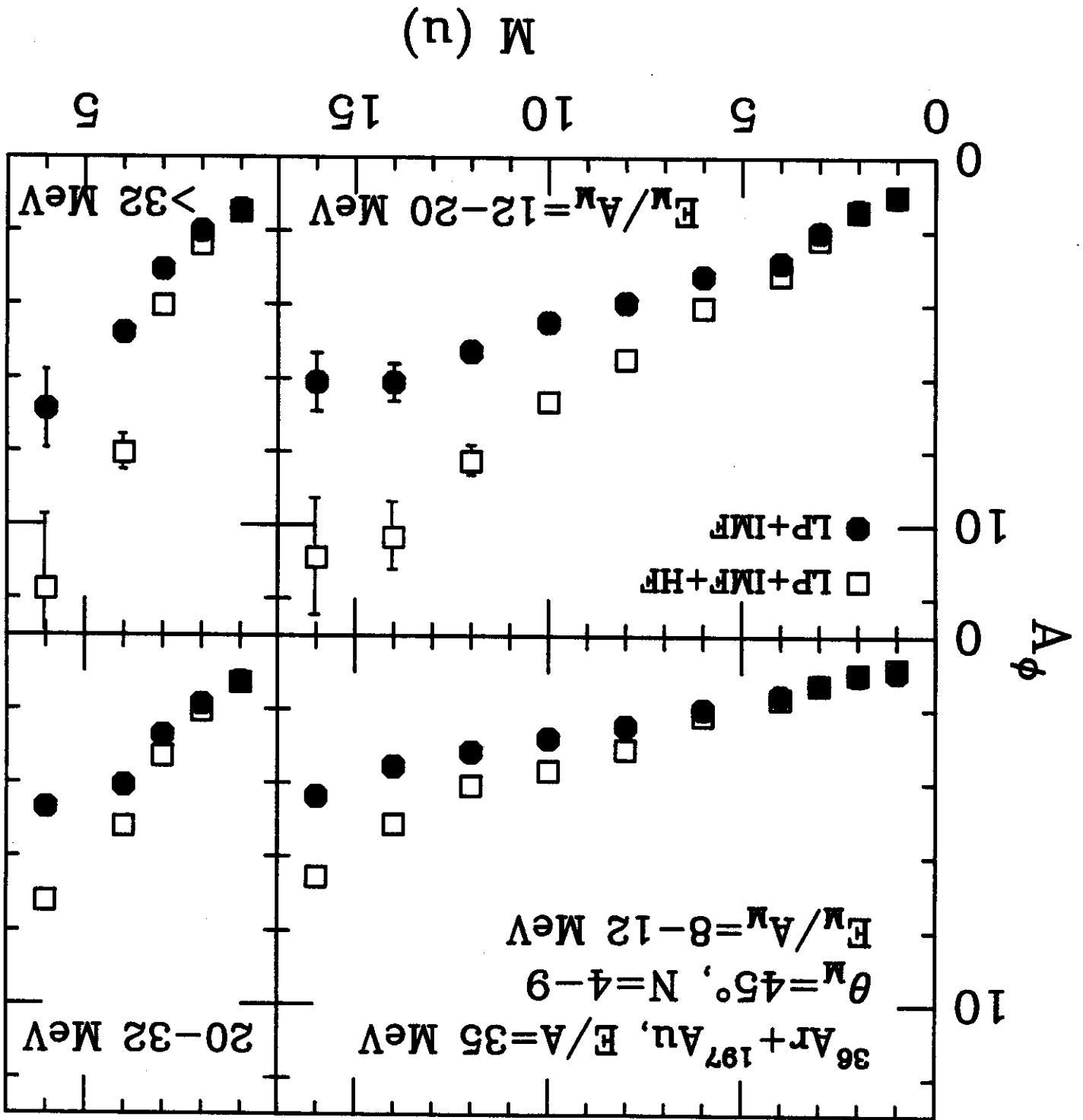


Fig. 13



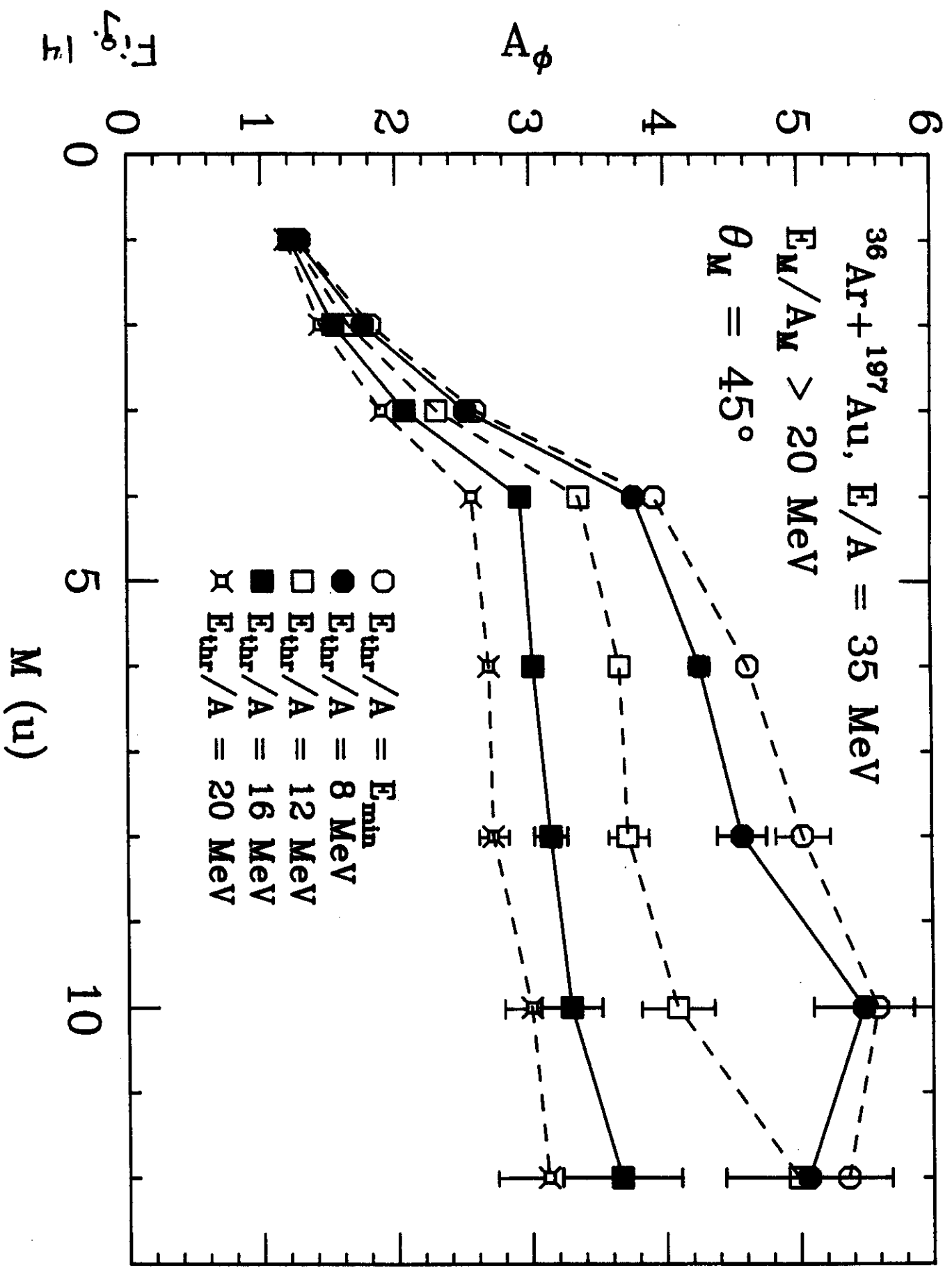


Fig. 14

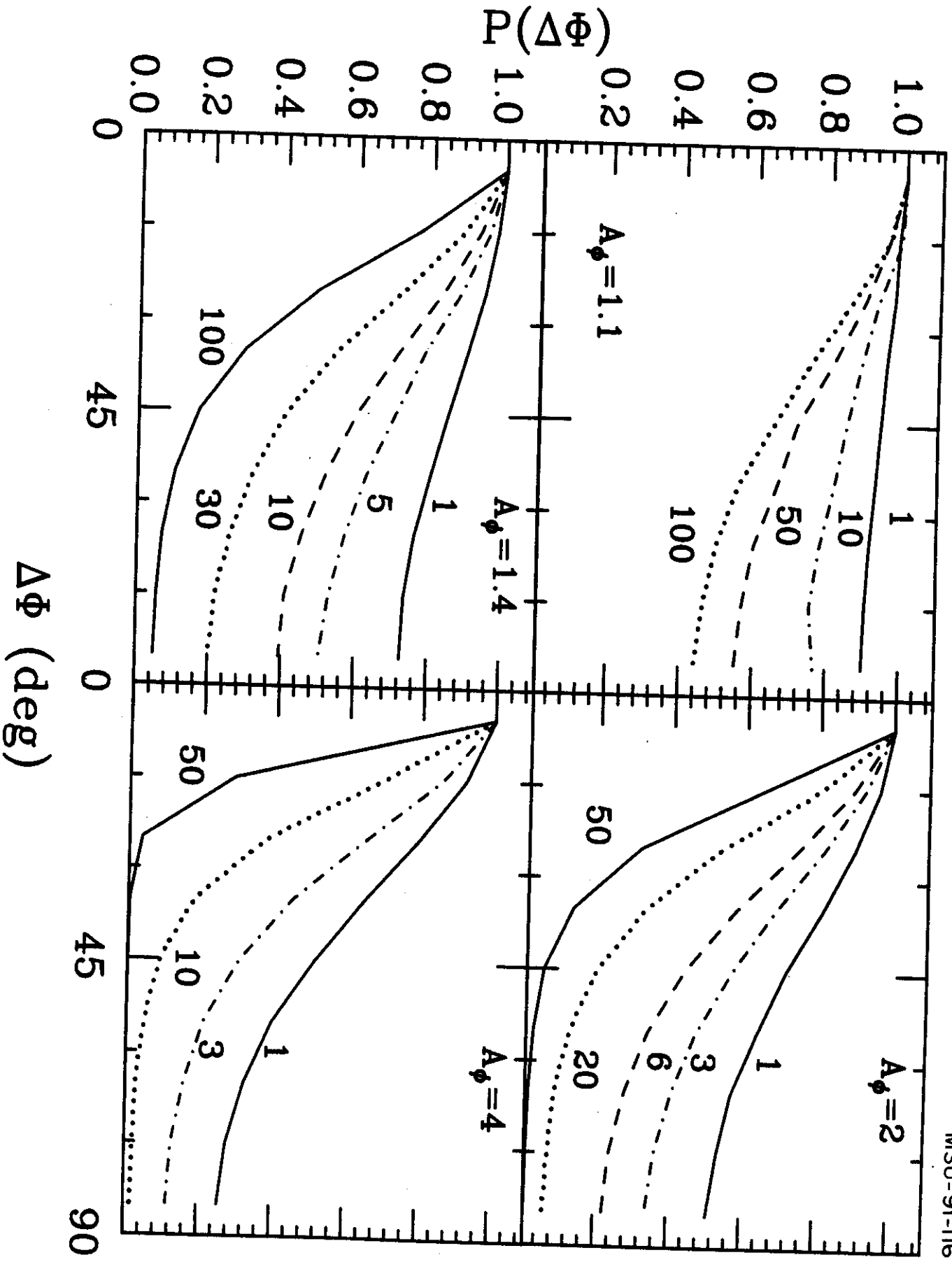


Fig. 15

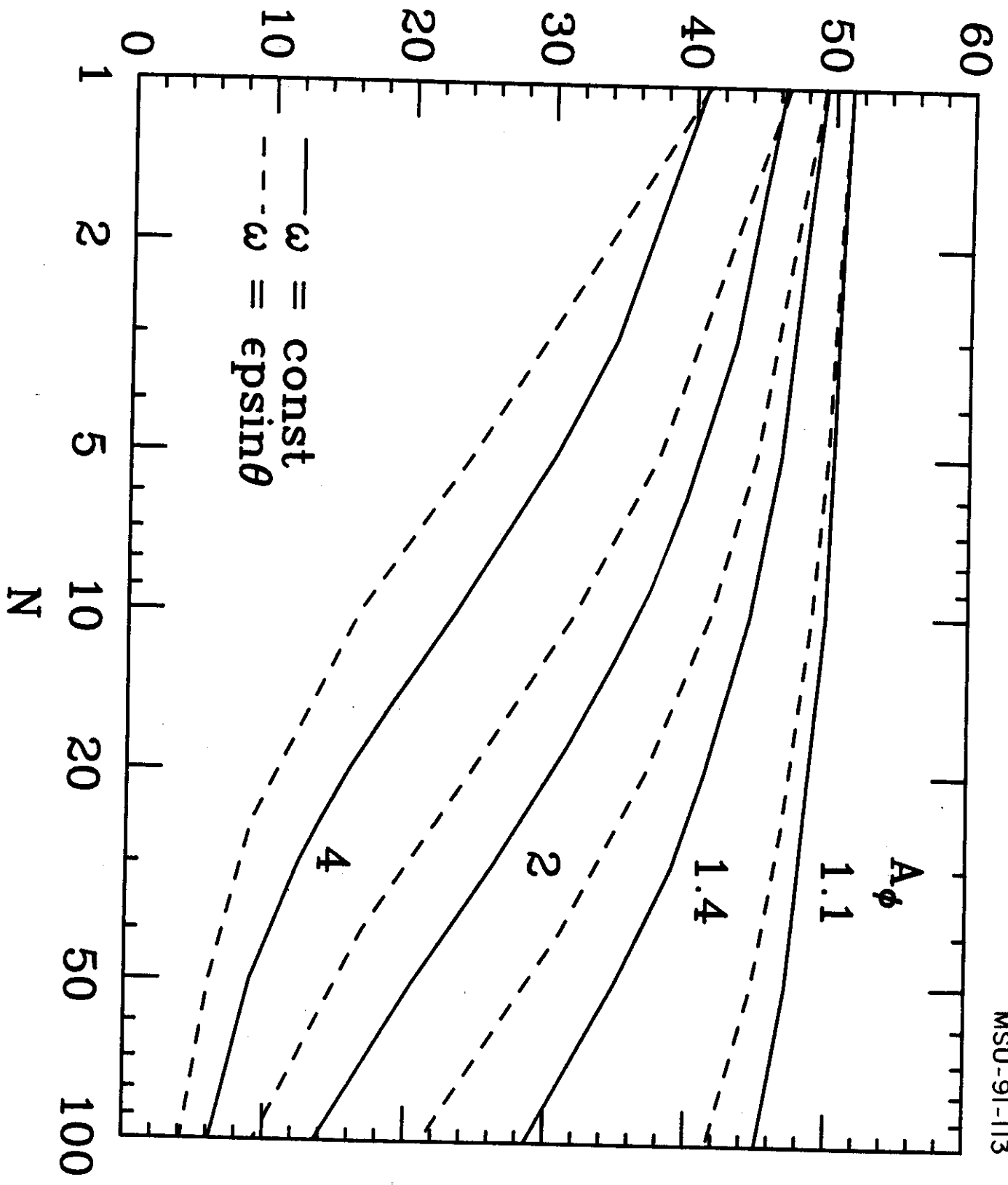


Fig. 16

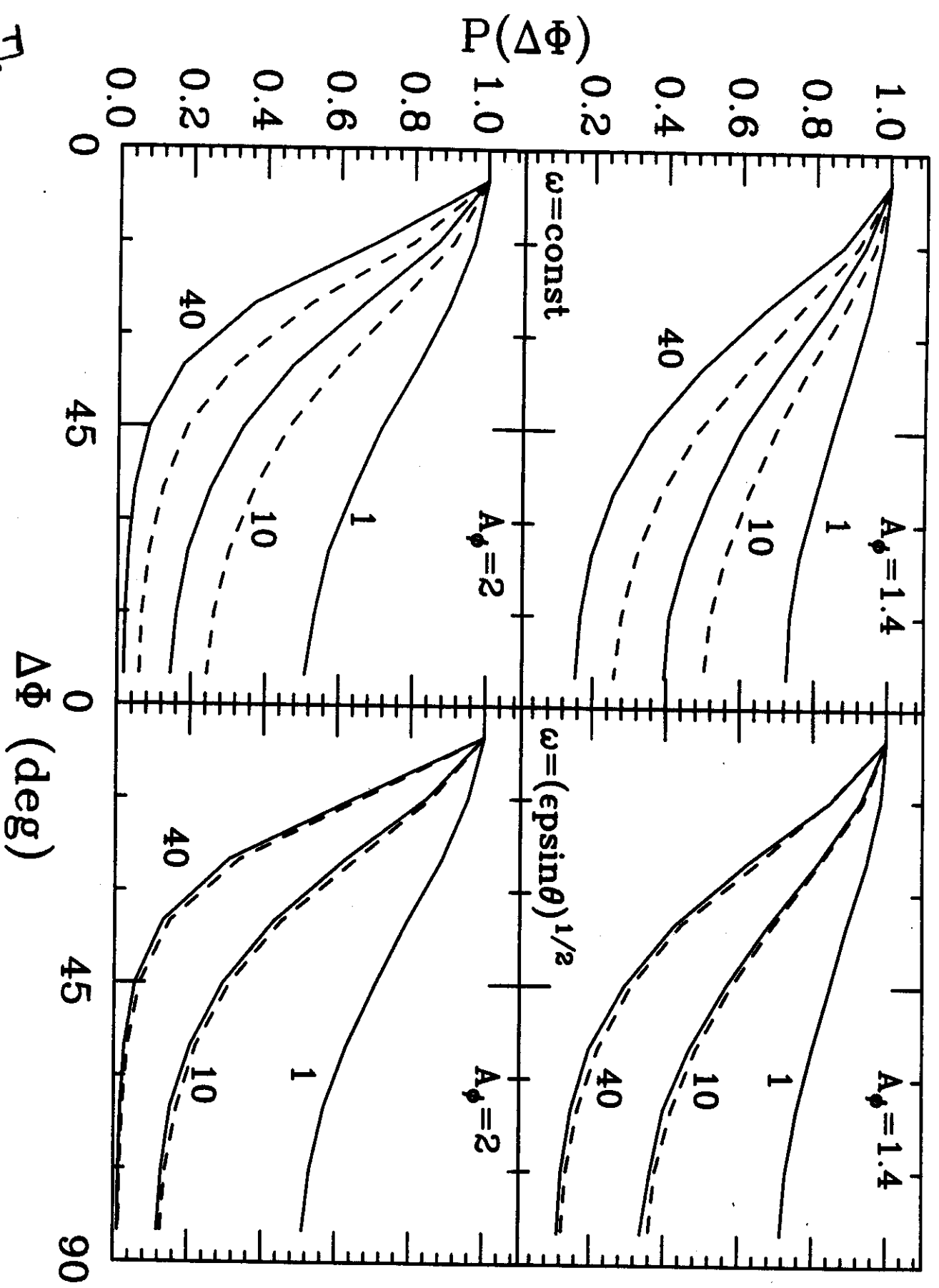


Fig. 17



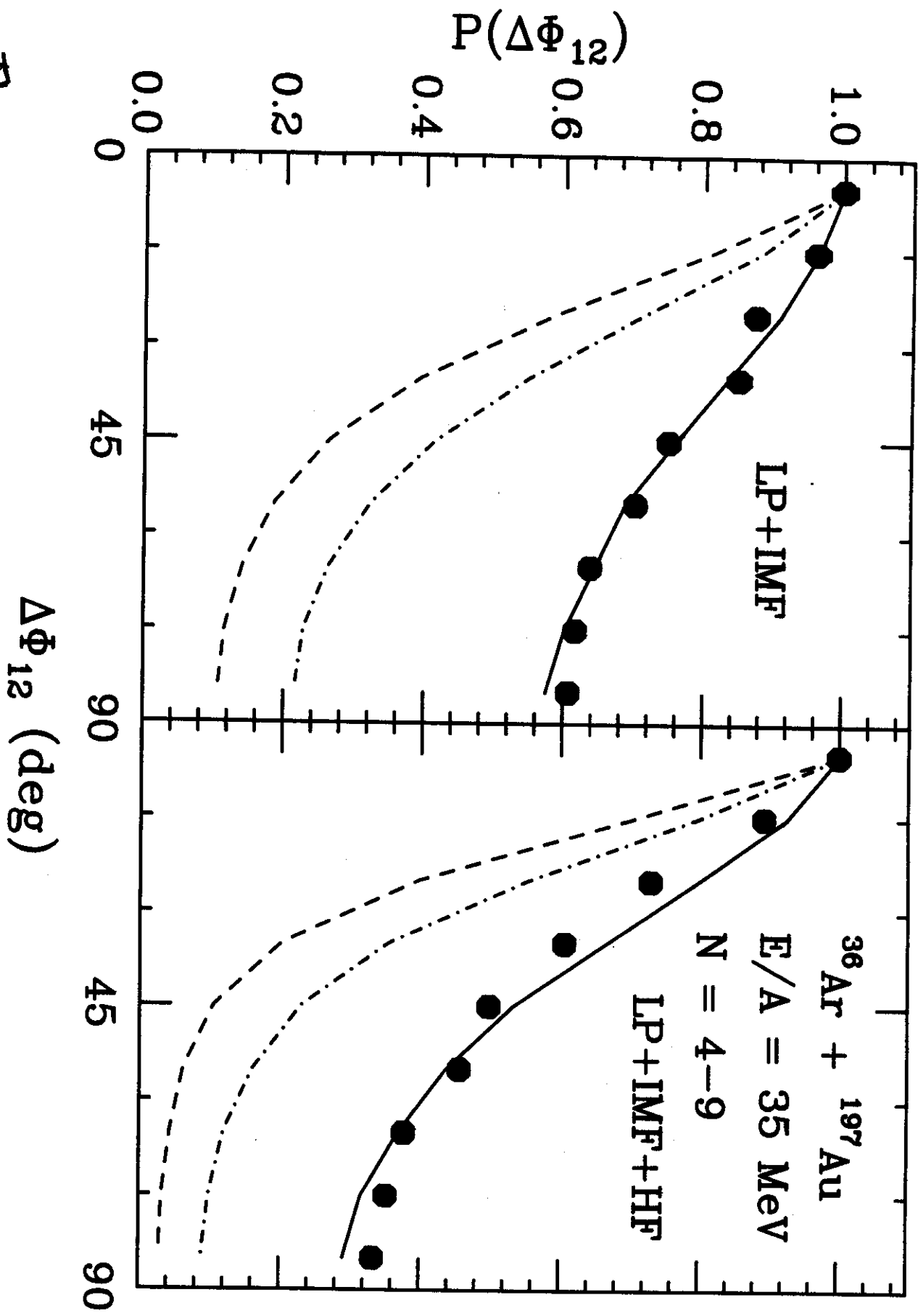


Fig 18

Fig 18

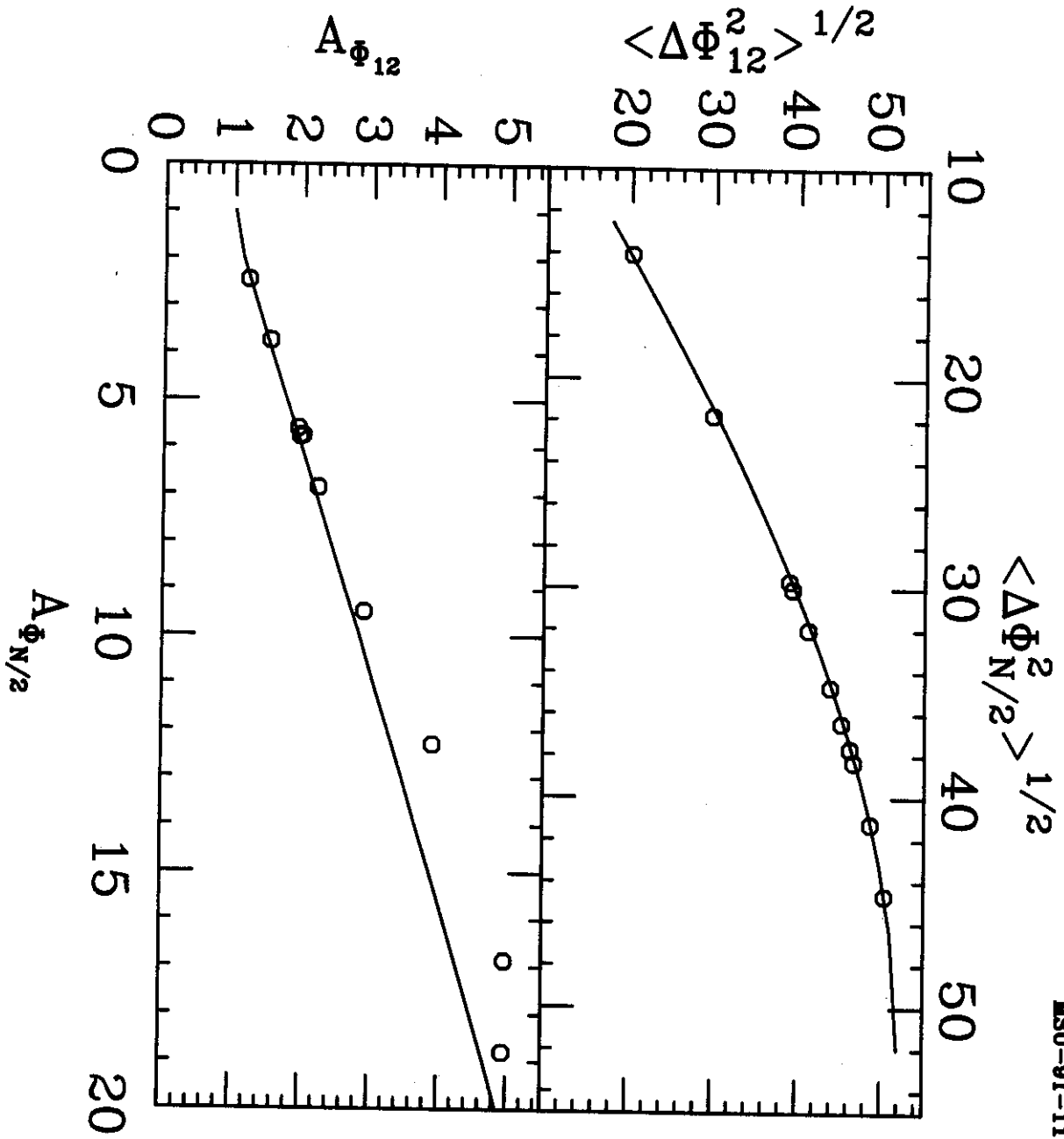


Fig 19

Fig. 2

$\langle \Delta\Phi_{N/2}^2 \rangle^{1/2}$  (deg)

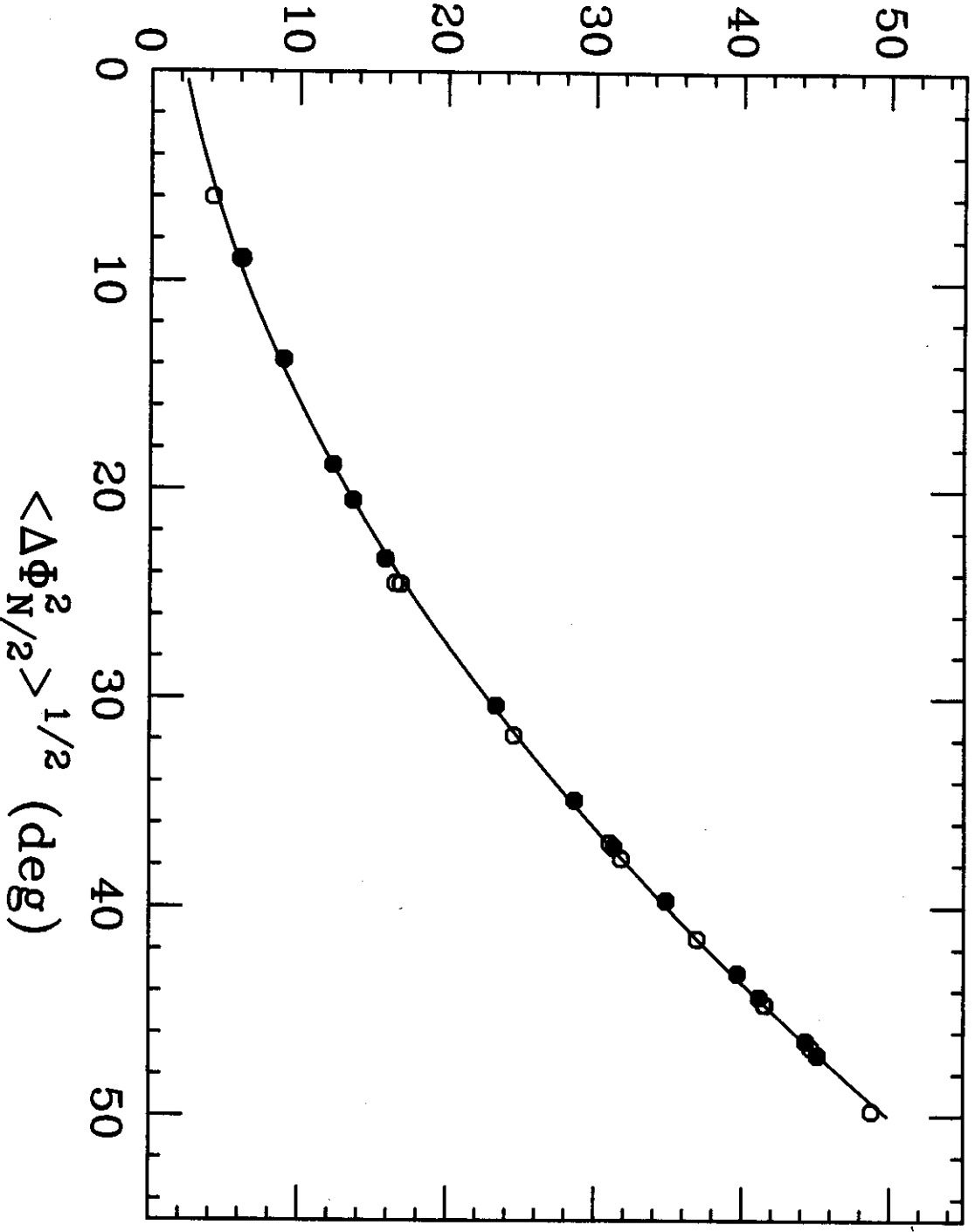


Fig 21

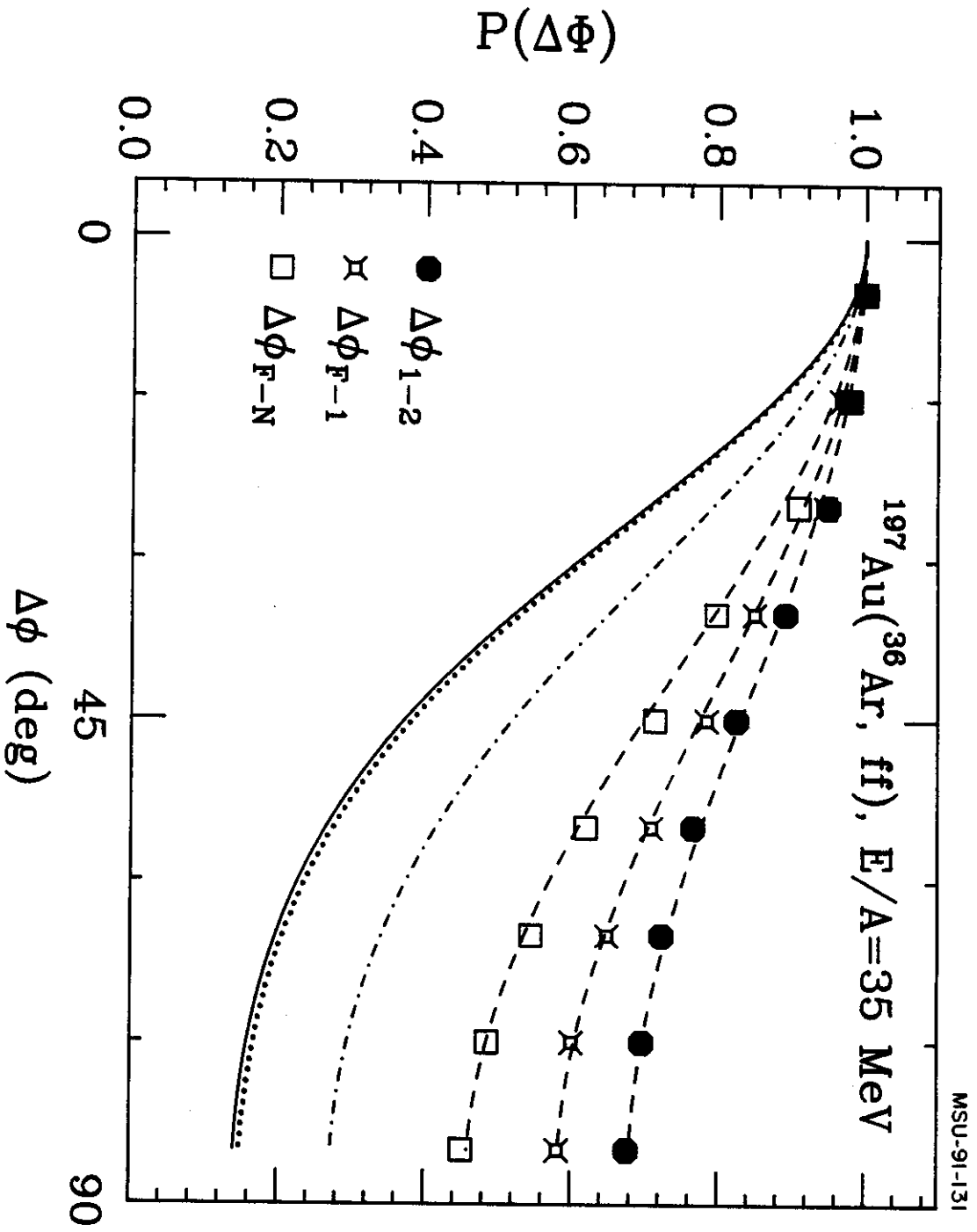
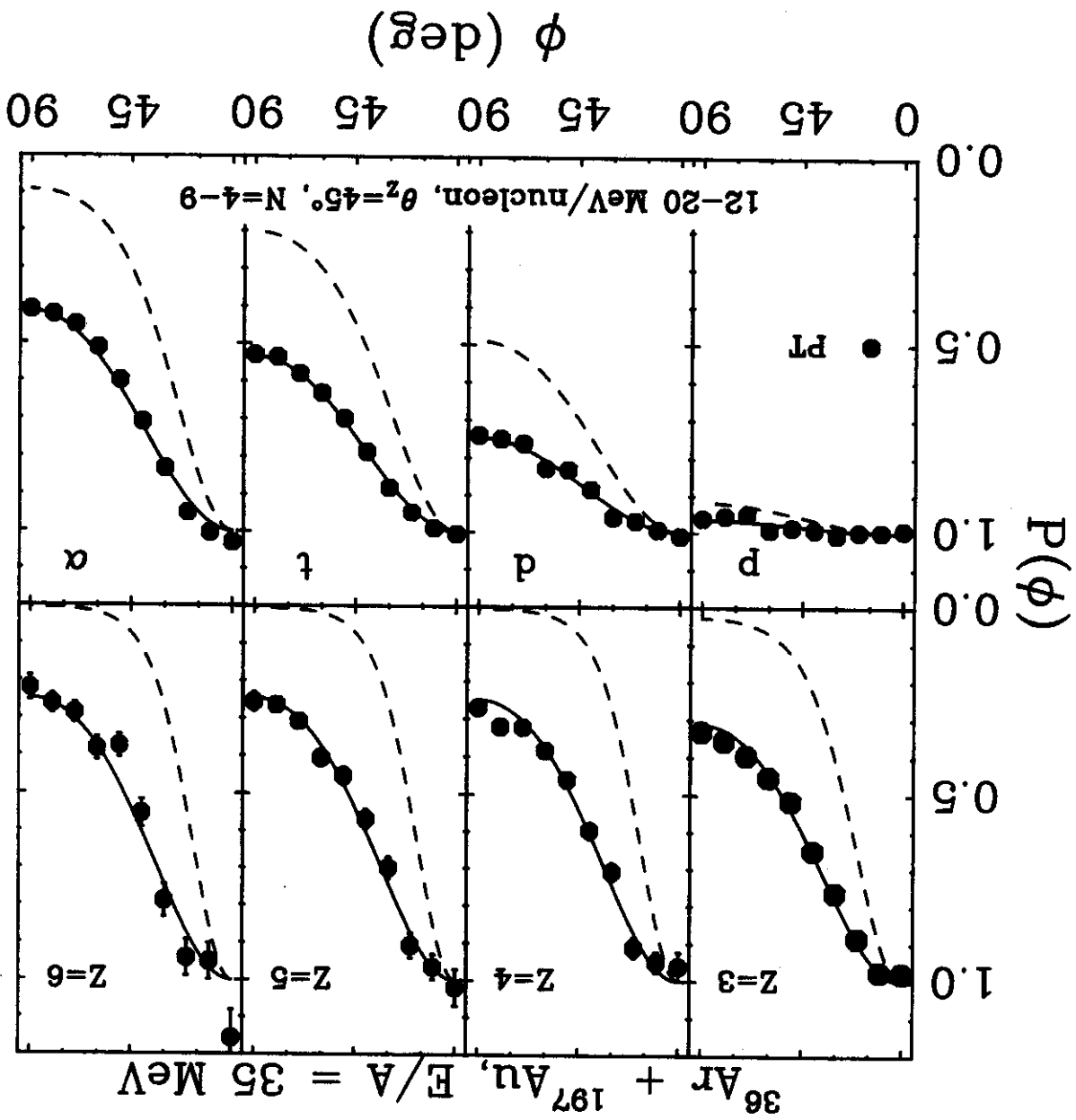


Fig 22



MSU-91-146